



## How a warmer Mediterranean preconditions the upper-level environment for the development of Mediane Ianos

Claudio Sánchez<sup>1</sup>, Suzanne Gray<sup>2</sup>, Ambrogio Volonté<sup>2,3</sup>, Florian Pantillon<sup>4</sup>, Ségolène Berthou<sup>1</sup>, and Silvio Davolio<sup>5</sup>

<sup>1</sup>MetOffice, Exeter, United Kingdom

<sup>2</sup>Department of Meteorology, University of Reading, UK

<sup>3</sup>National Centre for Atmospheric Science, University of Reading, Reading, UK

<sup>4</sup>LAERO, Université de Toulouse, CNRS, UPS, IRD, Toulouse, France

<sup>5</sup>ISAC-CNR, Bologna, Italy

**Correspondence:** Claudio Sánchez (claudio.sanchez@metoffice.gov.uk)

**Abstract.** Mediane Ianos in September 2020 was one of the strongest medicanes observed in the last 25 years. It was, like other medicanes, a very intense cyclone evolving from a baroclinic mid-latitude low into a tropical-like cyclone. The dynamical elements necessary to improve the predictability of Ianos are explored with the use of simulations with the Met Office Unified Model (MetUM) at 2.2 km grid spacing for five different initialisation times, from four to two days before Ianos's landfall.

5 Simulations are also performed with the Sea Surface Temperature (SST) uniformly increased and decreased by 2 K from analysis to explore the impact of enhanced and reduced sea-surface surface fluxes on Ianos's evolution. All the simulations with +2 K SST are able to simulate mediane Ianos, albeit too intensely. The simulations with control SST initialised at the two earliest times fail to capture intense preceding precipitation events at the right locations, and the subsequent development of Ianos. Amongst the simulations with -2 K SST, only the one initialised at the latest time develops the mediane.

10 Links between sea-surface fluxes and upper-level baroclinic processes are investigated. We find (i) a bubble of low-valued potential vorticity (PV) formed within a trough above where Ianos developed, diabatic processes associated with a preceding precipitation event triggered a balanced divergent flow in the upper-levels which contributed to the creation and maintenance this low-PV bubble, as shown by results from a semi-geostrophic inversion tool, (ii) Upper-level geostrophic vorticity advection associated with the low-PV bubble forced quasi-geostrophic ascent during Ianos's cyclogenesis, and (iii) diabatic processes  
15 dominated by deep convection formed a vertical PV tower in Ianos and continued to produce diabatically-induced divergent outflow aloft, thus sustaining Ianos's development. Simulations missing any of these three elements do not develop mediane Ianos.

Our results imply that preceding convection was essential for the subsequent development of Ianos, highlighting the importance of the interactions between near-surface small-scale diabatic processes and the upper-level quasi-geostrophic flow. A  
20 warmer SST strengthens the processes and thus enables Ianos to be predicted in simulations initiated at the earlier times that failed to generate the mediane with control SSTs.



## 1 Introduction

The Mediterranean region is one of the most cyclogenetic areas of the world (Hoskins and Hodges, 2002; Wernli and Schwierz, 2006). The most intense cyclones there produce considerable hazards, such as heavy precipitation (Flaounas et al., 2022; Khodayar et al., 2018), extreme winds (Raveh-Rubin and Wernli, 2015; Lfarh et al., 2023) or coastal impacts from large sea-level anomalies (Lionello et al., 2019; Ferrarin et al., 2023). The region is also a climate change hot-spot with large projected changes in temperature and precipitation (Giorgi, 2006), which might alter the mechanisms of Mediterranean cyclones and their hazards.

Some of the most intense Mediterranean cyclones exhibit tropical-like characteristics such as a cloud-free eye and an axisymmetric warm core, and hence they are commonly termed “Mediterranean hurricanes” or “medicanes”. Cavicchia et al. (2014) developed a climatology of this phenomenon from the dynamical downscaling of a high resolution reanalysis. They concluded that medicanes occur one to three times per year, and their genesis is mostly in the western Mediterranean and in the region extending between the Ionian Sea and the North-African coast. Medicanes have a peculiar seasonal cycle, their peak is at the beginning of winter, a relevant number of events occur during autumn, a few over spring, and they have very low activity in summer. Hence, medicanes tend to occur when there is cold air aloft.

The genesis of medicanes is typically preceded by the intrusion of potential vorticity (PV) streamers (Homar et al., 2003; Carrió et al., 2017) and unlike tropical cyclones, which intensify via the Wind-Induced Surface Heat Exchange (WISHE, Emanuel (1986); Rotunno and Emanuel (1987)) mechanism, upper-level baroclinic forcing is essential for the intensification of medicanes (Mazza et al., 2017; Fita and Flaounas, 2018). However, there is no clear understanding of the relationship between surface sea fluxes and baroclinic forcing in the cyclone intensification. Miglietta et al. (2017) proposed a classification of medicanes according to their mechanisms: (A) those dominated by WISHE in their mature stage, (B) those where both mechanisms (WISHE and baroclinic instability) appear important even at later stages, and (C) a blend of the previous two where tropical transition and a dramatic intensification occurs after a short but intense interaction of the cyclone with an upper-level PV streamer. Fita and Flaounas (2018) quantified the development of the surface pressure tendency for a medicane in December 2005 and attributed its deepening to warming in the atmospheric column from diabatic heating and advection within the upper troposphere. A reduction of the PV streamer by a PV inversion technique suppressed the cyclogenesis of a medicane in the cases described in Homar et al. (2003) and Carrió et al. (2017).

In addition to the presence of PV streamers, the axisymmetric warm core development in a medicane also depends on Sea Surface Temperature (SST). The ensemble simulations of Noyelle et al. (2019), with different SST increases, relate the warm core strength to a linear increase of SST warming, using the tropical cyclone phase space diagnostics of Hart (2003), but reveal that the minimum pressure growth is non-linear with the SST increase. Miglietta et al. (2011) found that increasing SST leads to a deeper medicane, stronger surface wind speeds and longer life-time of the medicane tropical features.

A reliable prediction of medicanes and their hazards can be obtained from a Numerical Weather Prediction (NWP) model able to reproduce the cyclone intensification mechanisms adequately, and initialised from a realistic analysis. The predictability of seven medicanes was assessed in Di Muzio et al. (2019) with an operational ensemble NWP model; late forecasts initialised

when the storm had already developed were more accurate than earlier forecasts, with a sharp drop in predictability. A medicane in January 2014 was simulated by different NWP models by Cioni et al. (2016), their results were strongly affected by the choice of initial conditions.

Our present study details the representation of medicane Ianos, one of the strongest medicanes ever observed (Lagouvardos et al., 2022), in simulations carried out with a state-of-the-art NWP model. In order to explore which processes are more important for the conditioning of the medicane intensification, the simulations are initialised at different times, meaning that some processes conducive to Ianos development are explicitly simulated in simulations with earlier initialisation times, while they are incorporated into the initial state of simulations with later initialisation times. The study also includes simulations with perturbed SST to explore the impacts of enhanced and suppressed sea-surface fluxes. The role of the diabatic processes before and during Ianos's intensification is diagnosed with the use of the Semi-Geotriptic inversion tool (SGT, Cullen 2018), and the baroclinic forcing during Ianos cyclogenesis with the use of the Quasi-Geostrophic omega equation (QG, Davies 2015).

Details of our simulations, the SGT inversion tool, the QG omega equation plus other evaluation tools and the observational datasets employed are provided in 2. A synoptic overview of the Ianos case is given in 3. The results from the simulations are presented in section 4. The main conclusions of this study are described in section 5.

## 70 2 Methodology

Regional simulations of medicane Ianos are carried out with the Met Office Unified Model (MetUM) at 2.2 km horizontal grid spacing, see sub-section 2.1 for further details on the MetUM setup. The region chosen for the simulations, the so-called model domain, is a bespoke choice for the Ianos case. It extends from the Tyrrhenian Sea to to the Aegean Sea (Fig. 1) and encompasses the locations of Ianos' cyclogenesis over the Gulf of Sidra, its tropical transition over the Ionian Sea and its landfall on the Greek Ionian Islands. The model is run for five days and initialised every 12 hours from 00Z 14 to 00Z 16 September 2020. Two additional sets of simulations with all the different initialisation times are run with the SST increased and decreased by 2 K uniformly over the whole domain (termed +2 K SST and -2 K SST, respectively). The choice of two degrees is motivated by the maximum to minimum range of SST perturbations in the global ensemble system (Tennant and Beare, 2014), it is also an effective way to trigger or suppress near-surface diabatic processes which later create convection and thus maximise or minimise the role of diabatic processes. It does not aim to represent SST changes in the Mediterranean under climate change projections.

The simulations are driven, in terms of both initial data and boundary conditions, by the 6-hourly European Centre for Medium range Weather Forecasting (ECMWF) Integrated Forecasting System Analysis (IFS-AN), with the operational resolution and configuration as in September 2020 (cycle 47r1, ECMWF 2020). The IFS-AN is preferred to the fifth generation ECMWF atmospheric reanalysis (ERA5, Hersbach et al. 2020) for its higher resolution, 9 km compared to 25 km. It is also preferred to the internal MetUM analysis as the IFS-AN is more accessible and can be ingested by other regional NWP models, thus allowing our simulations to be reproduced with other models. Sea surface temperatures are prescribed at the start of the simulation, and are interpolated from the 1/20° Operational Sea Surface Temperature and Sea Ice Analysis (OSTIA, Donlon



et al. 2012). The soil moisture analysis comes from the Met Office analysis for land-model consistency; it is described in  
90 Gómez et al. (2020).

The dynamical fields of the simulations are evaluated against the IFS analysis described above. The precipitation is compared  
to the Integrated Multi-satellitE Retrievals for the Global PRecipitation Measurement (IMERG or GPM (Hou et al., 2014;  
Skofronick-Jackson et al., 2017), abbreviated as GPM hereafter). The GPM spatial and temporal resolution is  $0.1^\circ \times 0.1^\circ$   
and 30 min. respectively. The satellite product is calibrated with month-to-month gridded gauge data. The representation of  
95 precipitation by GPM over the Mediterranean region is considered accurate, but it underestimates precipitation over mountainous  
regions (Navarro et al., 2019). GPM tends to overestimate extreme precipitation events such as those associated with tropical  
cyclone Imelda (Sakib et al., 2021) and those above the 95% percentile over the Maritime Continent (Da Silva et al., 2021).

Tropical features in Ianos including the cloud-less eye and spiralling branches are explored with the help of the Satellite-like  
Imagery Simulator (SIMIM), the wrapper to pre-process, run and post-process the unmodified core of the Radiative Transfer for  
100 TIROS Operational Vertical Sounder version 12 (RTTOV Saunders et al. 2018), a fast radiative transfer model for simulating  
top-of-atmosphere radiances. Cyclone tracks are computed by a simple algorithm that tracks for the minimum pressure over  
a  $4^\circ \times 4^\circ$  box with its centre at the cyclone's previous location. Despite its simplicity, the obtained cyclone trajectories and  
minimum pressure compare well to those from more complex tracking algorithms such as the one used operationally by the  
Met Office for tropical cyclones, described in Heming (2017).

105 Medium complexity models are employed to understand the importance of surface fluxes and upper level baroclinicity  
in Ianos's intensification. The role of diabatic processes is explored with the Semi-Geotriptic inversion tool which derives  
the balanced ageostrophic wind solutions from the MetUM fields; the tool is described in further detail in sub-section 2.2.  
Quantification of the forcing from upper-levels is done via the Quasi-Geostrophic omega equation, detailed in sub-section 2.3.

## 2.1 MetUM

110 The MetUM is a seamless modelling framework for weather forecasting and climate prediction across scales (Brown et al.,  
2012). Our simulations use the MetUM regional setup at version 12.0 with a grid spacing of 2.2 km, 90 terrain-following verti-  
cal levels with model top at 40 km, a time step of 75 seconds and a regional configuration known as Regional Atmosphere and  
Land version 2 for the mid-latitudes (RAL2-M), described in Bush et al. (2023). The RAL2M configuration does not include  
any parametrization for convection, its boundary layer scheme blends a 1-D convection parametrization, suitable for large grid  
115 lengths, with a subgrid turbulence scheme suitable for large-eddy simulation (Boutle et al., 2014). These characteristics allow  
the model to explicitly resolve convective events and, in particular small-scale processes such as a cloud-less eye.

The main components of RAL2-M are the "Even Newer Dynamics for the General Atmospheric Modelling of the Envi-  
ronment" (ENDGAME) dynamical core (Wood et al., 2014), the single moment micro-physics scheme based on Wilson and  
Ballard (1999) with particle size distribution for rain from the rain-rate-dependent distribution of Abel and Boutle (2012), the  
120 "Suite Of Community RADIative Transfer codes based on Edwards and Slingo" (Socrates) radiation scheme (Manners et al.,  
2018), the Smith (1990) cloud scheme with empirical adjustments to cloud fraction based on Boutle and Morcrette (2010), the



zero lateral flux (ZLF) moisture conservation scheme of Zerroukat and Shipway (2017) and the Joint community land surface model (JULES, Best et al. 2011).

## 2.2 Semi-Geotriptic inversion tool

125 The Semi-Geostrophic (SG) balanced flow is derived from the primitive equations after applying the hydrostatic balance and the geostrophic momentum approximation. It is an accurate approximation to the 3-D compressible Euler equations on scales larger than the Rossby radius of deformation (Cullen et al., 2005; Cullen, 2018). The inversion tool is then a single timestep integration of the SG system, and is employed as a diagnostic tool to evaluate a trajectory from MetUM fields that is consistent with the maintenance of geostrophic and hydrostatic balance. The semi-geotriptic (SGT) model improves the semi-geostrophic  
 130 model by the inclusion of Ekman friction in the boundary layer (Beare and Cullen, 2010). In our study, the use of the SGT targets the role of diabatic processes in the upper troposphere, where there is minimum friction. We thus refer to the ageotriptic wind as the “ageostrophic wind”, and SemiGeotriptic as Semi-Geostrophic, more familiar concepts in the literature. The SGT inversion tool has been previously applied to quantify the importance of diabatic processes in model error growth over the North Atlantic (Sánchez et al., 2020). It can also be applied in the tropics using the weak-temperature gradient, as done in  
 135 Hardy et al. (2023) to explore the dynamics of synoptic vortices over the South China Sea.

The mathematical formulation of the SGT tool is detailed in Cullen (2018) and Sánchez et al. (2020). Here, it is described by eq. 1, a simpler formulation of the momentum equation combined with geotriptic and hydrostatic balance, derived in Cartesian coordinates. The Matrix Q shown in eq. 2:

$$\mathbf{Q} \begin{bmatrix} u - u_g \\ v - v_g \\ w \end{bmatrix} + \frac{\partial}{\partial t} (\nabla \phi) = \begin{bmatrix} -f \mathbf{u}_g \cdot \nabla v_g + f M2 \\ f \mathbf{u}_g \cdot \nabla u_g - f M1 \\ -\frac{g}{\theta_0} \mathbf{u}_g \cdot \nabla \theta + \frac{g}{\theta} S_\theta \end{bmatrix}, \quad (1)$$

$$140 \quad \mathbf{Q} = \begin{bmatrix} f^2 + f \frac{\partial v_g}{\partial x} & f \frac{\partial v_g}{\partial y} & f \frac{\partial v_g}{\partial z} \\ -f \frac{\partial u_g}{\partial x} & f^2 - f \frac{\partial u_g}{\partial y} & -f \frac{\partial u_g}{\partial z} \\ -\frac{g}{\theta_0} \frac{\partial \theta}{\partial x} & -\frac{g}{\theta_0} \frac{\partial \theta}{\partial y} & -\frac{g}{\theta_0} \frac{\partial \theta}{\partial z} \end{bmatrix}, \quad (2)$$

where  $\mathbf{u}_g = (u_g, v_g)$  denotes the geostrophic wind,  $\phi$  the geopotential,  $\theta$  the potential temperature with  $\theta_0$  the environmental value, and  $f$  the Coriolis parameter. Momentum forcing from gravity wave drag, boundary-layer or convection parametrization is represented by the  $(M1, M2)$  vector and the diabatic forcing from MetUM parametrizations as  $S_\theta$ . Note, in this study we neglect the momentum terms (M1 and M2), in line with Sánchez et al. (2020), and only consider diabatic forcing from  
 145 the radiation, large-scale precipitation, cloud and boundary layer MetUM parametrizations. As mentioned above, there is no convection scheme in the RAL2M MetUM configuration, so the temperature changes during convective ascents are represented by the other parametrizations.

The SGT forcing is on the right hand side of equation 1. The first term represents the geostrophic forcing, and the second term the diabatic forcing coming from subgrid parametrizations. Either of these terms can be set to zero in the SGT inversion



150 tool. For the cases where the SGT is forced by the geostrophic term only, hence  $S_\theta = 0$ , we term the SGT inversion tool solution *NO – HEAT*. For the cases where the geostrophic forcing is set to zero and only the diabatic term is applied, the solution is termed *HEAT – ONLY*; this solution represents the balanced flow induced by diabatic heating.

MetUM prognostic fields and tendencies from the physics schemes are outputted every 6 hours for the SGT inversion tool. To filter the scales below the Rossby radius of deformation, the discrete cosine filtering technique of Denis et al. (2002) is  
155 applied to filter wave-numbers above 50, equivalent to a wavelength of  $0.32^\circ$ . The fields are then bi-linearly regridded to a  $1.5^\circ \times 1.5^\circ$  latitude-longitude mesh before they are read in by the SGT inversion tool.

### 2.3 Quasi-Geostrophic omega equation

The SGT inversion tool currently has no capacity to restrict the forcing terms to certain levels. The Quasi-Geostrophic (QG) omega equation on the other hand allows height-attributable solutions, which have been applied to the classification of extra-  
160 tropical cyclones according to the contribution from upper or lower levels in their development (Deveson et al., 2002; Plant et al., 2003; Gray and Dacre, 2006). Moreover the QG omega equation is conceptually simpler as well as more commonly used in the literature, and so it is used here to understand the role of upper-level baroclinicity (without the inclusion of diabatic forcing) in the development of Ianos.

The QG system is based on a first order approximation of the primitive equations with a small Rossby number. It prescribes  
165 the ageostrophic vertical velocity required by the prevailing geostrophic flow to maintain geostrophic balance. The QG system is simpler than the SG system: it assumes uniform static stability on each level whereas the SG system allows horizontal gradients of static stability. Additionally the QG system only allows advection of temperature and momentum by the geostrophic wind, whereas the SG system also allows advection by the ageostrophic velocity. For further details on the differences between the SG and QG systems see section 2.3 of Sánchez et al. (2020).

170 The QG omega equation has been extensively used to examine the large-scale vertical velocity patterns of atmospheric systems. It has several formulations, detailed in Davies (2015). The conventional formulation is shown in eq. 3, where  $\sigma$  is the static stability,  $\zeta_g$  is the relative geostrophic vorticity and  $\phi$  the geopotential. The first term on the right-hand-side is commonly referred as the geostrophic Vorticity Advection term (VA), and the second as the Thermal Advection term (TA). Forcing from VA is assumed to dominate the QG forcing at upper levels yielding the upper-level forced ascent (Deveson et al., 2002).

$$175 \left( \sigma \nabla^2 + f_0^2 \frac{\partial^2}{\partial p^2} \right) \omega = f_0 \frac{\partial}{\partial p} [v_g \cdot \nabla (\zeta_g + f)] + \nabla^2 \left[ v_g \cdot \nabla \left( -\frac{\partial \phi}{\partial p} \right) \right] \quad (3)$$

The QG inversion tool cannot achieve convergence with MetUM fields on their 2.2km native grid. Hence, the MetUM horizontal winds,  $\theta$  and  $\phi$  fields are spectrally truncated to wave-number 16, equivalent to  $1^\circ$ , using the Discrete Cosine Function (DCT) of Denis et al. (2002). In order to minimise the Gibbs phenomenon, the DCT includes the smoothing spectral filter of Sardeshmukh and Hoskins (1984).



### 180 3 Case Description

Medicane Ianos travelled from the Gulf of Sidra to the Greek Ionian islands between 15 and 18 of September 2020. Ianos started its cyclogenesis on 15/9 over anomalously warm waters at 28°C, 1.5 K to 2.0 K warmer than the 1985-2005 climatology (Lagouvardos et al., 2022; Zimbo et al., 2022). The environment was dominated by a cut-off low above the Gulf of Sidra, isolated from the Atlantic flow on the 11/9, and a series of intense but disorganised co-located convection events on the 13 and 14 (Zimbo et al., 2022). Ianos intensified and attained a full tropospheric warm core at 03Z 17, as shown in cyclone phase space diagrams of Zimbo et al. (2022). It initially travelled northwards on the 16 across the Ionian Sea towards Southern Italy, and eastwards afterwards till landfall over the Greek Ionian Islands at 06Z 18, with maximum wind gust of 50 m/s recorded at Palliki station in North Kefalonia, and daily accumulated rainfall of 644.7 mm in Antipata, at the northernmost part of Kefalonia. Diakakis et al. (2023) records Ianos' impacts on geomorphology and infrastructure on the Ionian islands. On the following days after landfall, Ianos headed south and started to weaken; it lost its tropical characteristics around 00Z 19. The trajectory of the IFS analysis is shown in Fig. 1. Table 1 briefly describes Ianos's evolution.

| Day      | Description  |
|----------|--|
| 11 to 15 | Strong convective precipitation in the Gulf of Sidra below a cut-off low.  |
| 15       | Ianos's cyclogenesis over the Gulf of Sidra with 28°C SST, 2 K above climatology.  |
| 16       | Ianos moves north while it intensifies. PV streamer wraps around the cyclone on the 335K isentrope at 12Z.   |
| 17       | Ianos develops a warm core and an eye with intense convection and wind gusts around the eye. Ianos moves eastwards towards the Greek Ionian Islands. |
| 18       | Ianos hits the Greek Ionian Islands in western Greece: daily accumulated precipitation peaks above 600 mm and wind gusts above 50 m/s.               |
| 19       | Ianos moves south towards Levant and decays, losing its tropical-like features   |

**Table 1.** Brief timeline of the development of Ianos and its preceding events on September 2020.

## 4 Results

### 4.1 Ianos's track and intensity

The minimum Mean Sea Level Pressure (MSLP) along Ianos's trajectory from analyses and MetUM simulations is shown in Figure 2, with the minimum pressure observed at Palliki station in Kefalonia (Greece) at landfall reported in Lagouvardos et al. (2022). The cyclone starts to intensify in the analysis at 00Z 15 and at a faster rate from 00Z 16. It peaks on the 17<sup>th</sup> when it becomes a medicane, and then it starts to decay sharply after landfall at 06Z 18. Both the IFS and MetUM analyses are 5 hPa and 10 hPa weaker respectively than the observed value at Palliki station at 03Z 18, despite the location offset of the station to the cyclone's minimum pressure location. Tropical cyclone warning centres around the globe (e.g., the Japan Meteorological

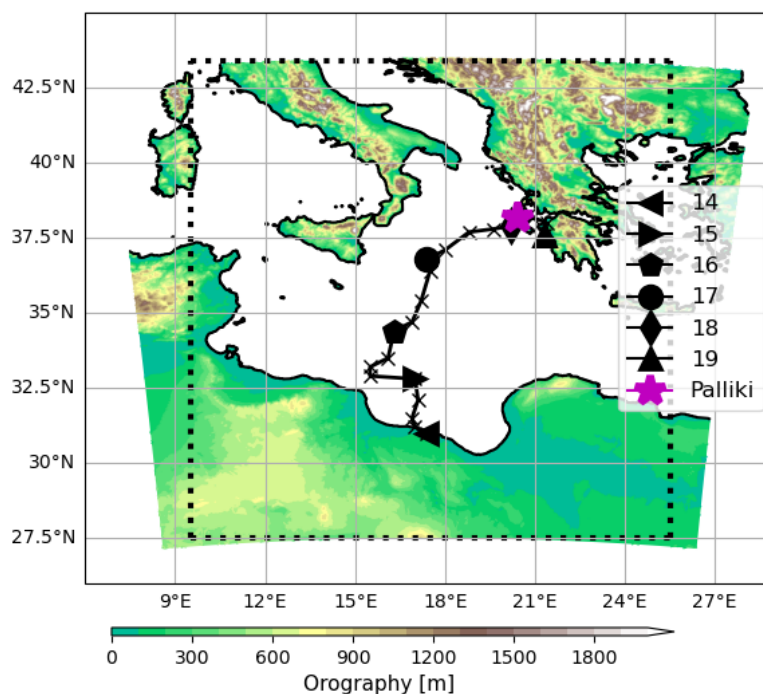


**Figure 1.** Domain for the 2.2km MetUM simulations and its orography (coloured). The black dotted box represents the area where Ianos is evaluated in the MetUM simulations. Ianos's trajectory from the IFS analysis is represented by the black line, with crosses every 6 hours and different symbols for different days in September 2020 at 00Z; only points with surface pressure below 1012 hPa are shown. The magenta asterisk denotes the location of Palliki Station in Kefalonia.

200 Agency and the National Hurricane Center) produce estimates of the intensities of cyclones which are assimilated by models such as the IFS (Heming, 2016). However, there is no official warning centre for Mediterranean cyclones and thus the weaker intensities in the analyses could be the result from the lack of central pressure estimates.

All the five simulations with +2 K SST develop a strong Ianos (copper lines of different shadings and symbols in Fig. 2), reaching a minimum MSLP of 950–960 hPa. For the subset of simulations with control SST, only those initialised at and after  
205 00Z 15 capture the intensification of Ianos (green lines with circles, diamonds or crosses in Fig. 2), with a range of maximum intensities of 970–985 hPa. There is only one simulation with -2 K SST capturing Ianos's intensification albeit weakly, the one initialised at the latest time: 00Z 16 (pale blue line with crosses in Fig. 2). The earlier the simulations with +2 K SST are initialised, the deeper their cyclone becomes (e.g. copper-shaded lines with dots and crosses in Fig. 2), probably the result  
210 to simulate Ianos produce stronger intensities for later initialisation times (shorter lead times). The lack of cooling feedback



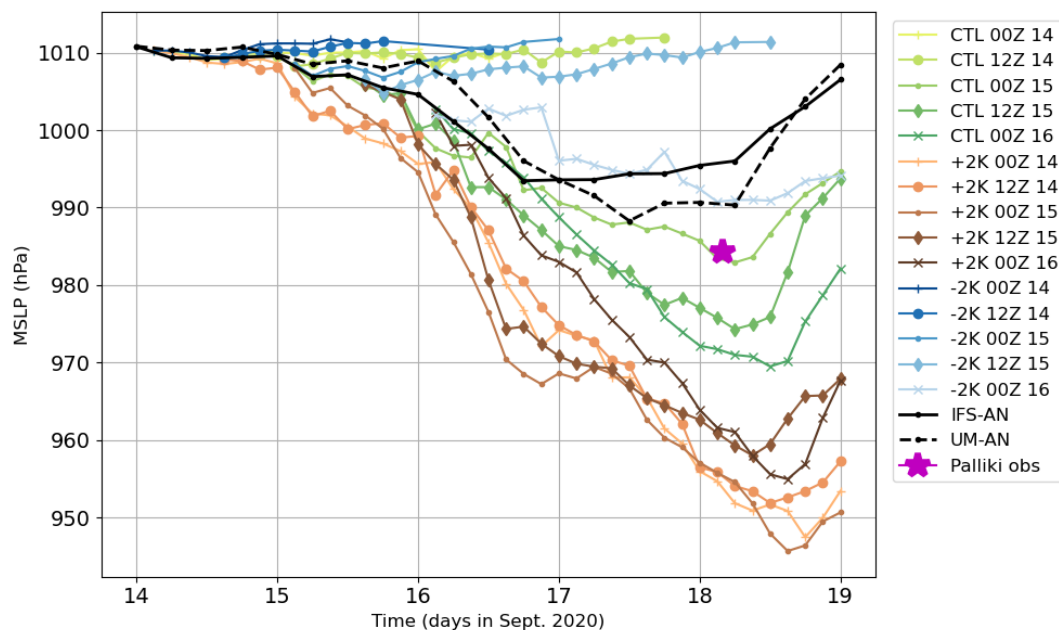


**Figure 2.** Ianos’s MSLP evolution from 14–19 September for the IFS analysis (black dashed), the MetUM analysis (black dotted), and all MetUM simulations (green for control, copper for +2 K SST and blue for -2 K SST). Simulations initialised at an earlier time are represented by darker colours and different symbols. The magenta star denotes the observed minimum MSLP at the Palliki Station in Kefalonia. Only points below 1012 hPa are shown. The first point in the simulations corresponds to a 3 hour leadtime forecast (denoted T+3).

in these prescribed SST simulations may produce an over-intensification of Ianos, as is common with tropical cyclones in simulations uncoupled to ocean models (e.g Short and Petch 2018; Castillo et al. 2022).

The trajectory differences amongst simulations are less structured than those for the intensities. Their differences to the IFS analysis in terms of latitude and longitude are shown in Fig. 3. In the simulations where Ianos does not intensify and remains a rather weak mid-latitude low (above 1008 hPa), it does not travel as far north as it does in the simulations where it rapidly intensifies and attains tropical-like features; e.g. the control simulation initialised at 00Z 14 (olive-green pluses) and 12Z 14 (olive-green circles), or the simulation with -2 K SSTs initialised at 12Z 15 (pale-blue diamonds). Most of the simulations show a 1° western bias emerging on the 17<sup>th</sup>, indicating that the cyclone is slower in the simulation than in the analysis, a positional bias leading to a later landfall and hence give Ianos more time to be fed by sea-surface fluxes which may explain why Ianos’s minimum surface pressure is reached about one day later in the simulations than in the analyses (Fig. 2).

Despite the different intensities, all the simulations initialised at the latest initialisation date, 00Z 16, show a medicane with a tropical-like structure at 06Z 18 denoted by a cloud-less eye and spiralling branches in Fig. 4 which shows the simulated satellite Brightness Temperature ( $T_b$ ) at 10.8  $\mu\text{m}$  obtained from the satellite-like imagery simulator SIMIM. For reference, Zimbo et al. (2022) observed  $T_b$  216 K at 03Z 18 (equivalent to the lighter white colours in Fig. 4). The simulation with +2 K

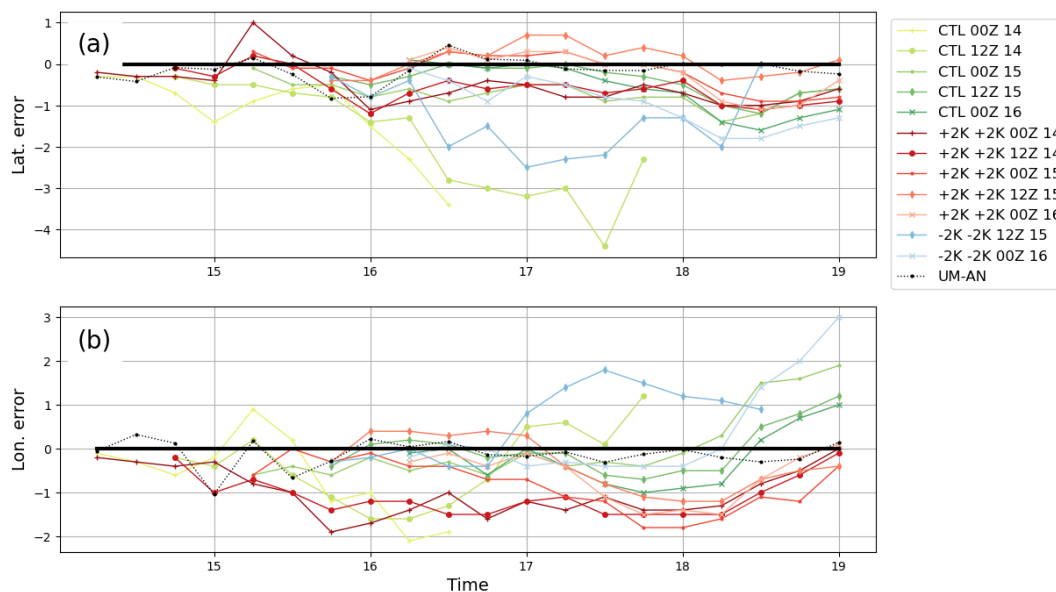


**Figure 3.** Ianos’s trajectory errors compared to the IFS analysis for the different simulations in (a) latitude (b) longitude. Same colour legend as in Fig. 2.

225 SST generates the largest and strongest Ianos (Fig. 4.a), extending about 500 km, with the lowest  $Tb$  and thus highest cloud tops. In the simulation with -2 K SST Ianos still shows the eye and spiralling branches (Fig. 4.c), but it is much smaller in size and its higher  $Tb$  indicates weaker convective activity.

#### 4.2 Evolution of Precipitation

Heavy precipitation occurred over the Gulf of Sidra and the southwest sector of the Ionian Sea before Ianos’s cyclogenesis. It was of convective nature and quite disorganised despite being fairly intense (Zimbo et al., 2022). One possible mechanism for the thunderstorm development is so-called "dry-eyes", where stratospheric intrusions into the lower troposphere are shown as isolated dark spots on the water vapour channel of the satellite imagery, triggering potential instability and thus convection (Roberts, 2000). Dry eyes were observed over the region on the 13<sup>th</sup> in the water vapour channel ( $6.25\mu$ ) by the Spinning Enhanced Visible and InfraRed Imager (SEVIRI) instrument on board of the Meteosat Second Generation Satellite (MSG, not shown but available at the NCAS British Atmospheric Data Centre 2006).

The satellite-derived product GPM shows intense precipitation over the Gulf of Sidra between 12Z 14 and 12Z 15 (Fig. 5.a). The precipitation location over this period is spatially collocated with Ianos’s trajectory downstream between 00Z 15 and 06Z 16 (right-ward arrow and pentagon symbols in Fig. 5.a). From all three simulations initialised at 00Z 14 only the one with +2 K SST captures the location of the preceding rainfall downstream of the cyclone (Fig. 5.b). The simulation with control SST initialised at 00Z 14 produces much weaker accumulated precipitation over the same time and location as GPM (Fig. 5.c),

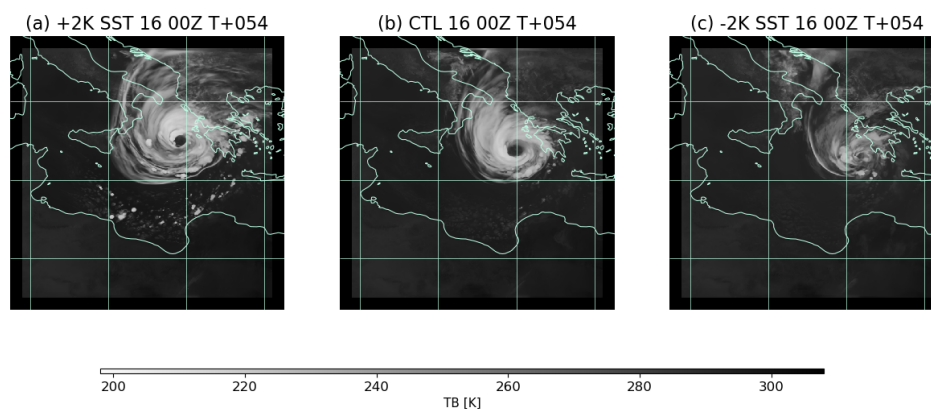


**Figure 4.** Brightness Temperature from the SIMIM satellite simulator at  $10.8 \mu\text{m}$ , validation time for 6Z 18/9 (a) control (b) +2 K SST and (c) -2 K SSTs simulations, all initialised at 00Z 16.

but slightly stronger precipitation over the Tunisian coast. Ianos does not travel over the area with preceding precipitation until 00Z, 16, a day later than when it occurs in GPM or the equivalent simulation with +2 K SST. The -2 K SST simulation has nearly absent precipitation over the Gulf of Sidra (Fig. 5.d), probably the result of weaker surface fluxes reducing the thermal vertical gradient and suppressing convective activity over the sea.

245 The evolution of 6-hourly accumulated precipitation along the cyclone trajectory is shown in Figure 6, the time-series of the domain averaged precipitation over a  $3 \times 3^\circ$  box with the cyclone at the centre. The GPM satellite product shows two maxima in precipitation around the cyclone. The first at 00Z 15 is the preceding precipitation event over the Gulf of Sidra shown in Fig. 5, when Ianos is just a weak small perturbation in the surface pressure field; this peak is refereed as preceding precipitation or peak “A” hereafter. The second maximum is at 12Z 16 when Ianos is undergoing a rapid intensification; it is  
250 refereed as Ianos intensification precipitation peak or peak “B” hereafter. Other medicanes also show the equivalent to Ianos’s peak “B”, producing intense precipitation, lighting and deep convection 12–24 hours ahead of achieving medicane status with tropical-like features (Miglietta et al., 2013; Fita and Flaounas, 2018).

The simulations with +2 K SST are the only ones capturing both precipitation peaks, although they also develop a spurious third peak at 12Z 18 (Fig. 6). This third peak comes from a later landfall and thus a higher exposure to the warmer SST (Figs  
255 3 and 5.a,b). The simulations with +2 K SST initialised at 12Z 15 and 00Z 16 follow a similar pattern to the ones initialised at earlier times and are not shown. The precipitation timeseries in the simulations with control SST initialised on the 14<sup>th</sup> miss peak “A” (olive-green lines with circles and pluses in Fig. 6), but in these simulations the precipitation increases at about the same rate on the 15<sup>th</sup> as the other simulations with control SST which are able to develop Ianos. However, in those missing Ianos’s intensification, the precipitation rate drops after reaching its maximum early in the 16<sup>th</sup> whereas in those simulations  
260 initialised afterwards, and capturing Ianos intensification, there is ongoing precipitation after peak “B” (Fig. 6). The simulations

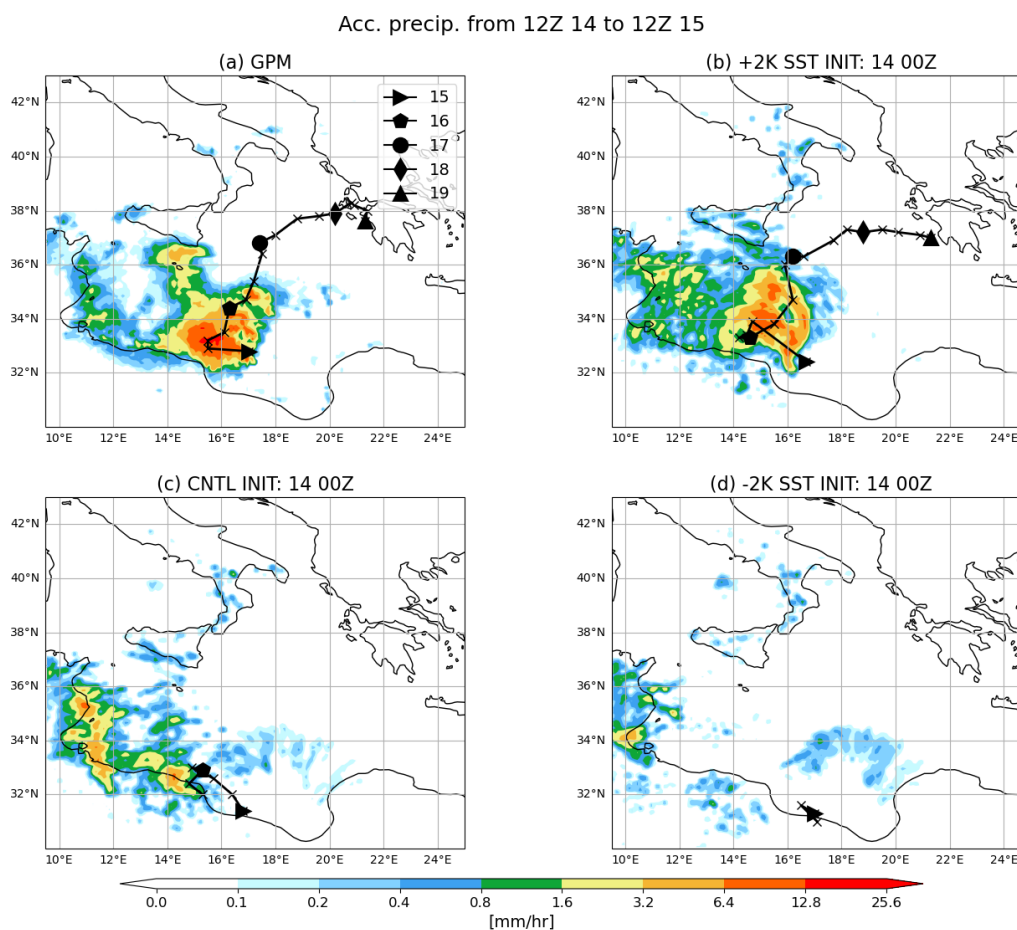


**Figure 5.** Daily accumulated precipitation from 12Z 14 to 12Z 15 for (a) GPM, and simulations initialised at 00Z 14: (b) Control (c) +2 K SST (d) -2 K SST. Black line denotes the cyclone tracks of the IFS analysis in (a) and simulations in (b–d) with crosses every 6 hours and different symbols for different days in September 2020 at 00Z from 00Z 15, only values below 1012 hPa are shown.

initialised at and after 12Z 15 follow a similar pattern to the one initialised at 00Z 15 and are not shown. Most of the simulations with -2 K SST produce negligible precipitation with the exception of the ones initialised at the latest two times (not shown). Only the latest one (initialised at 00Z 16) produces a tropical-like cyclone Ianos and substantial precipitation along its track, whereas the one initialised 12 hours earlier (at 12Z 15) produces a drop in the intensity and precipitation within a few hours (blue line with diamonds in Figs 2 and 6 respectively). The moisture availability in the lower levels is substantially reduced compared to the control simulations due to the small values ( $< 150W/m^2$ ) of latent heat fluxes (not shown).

265

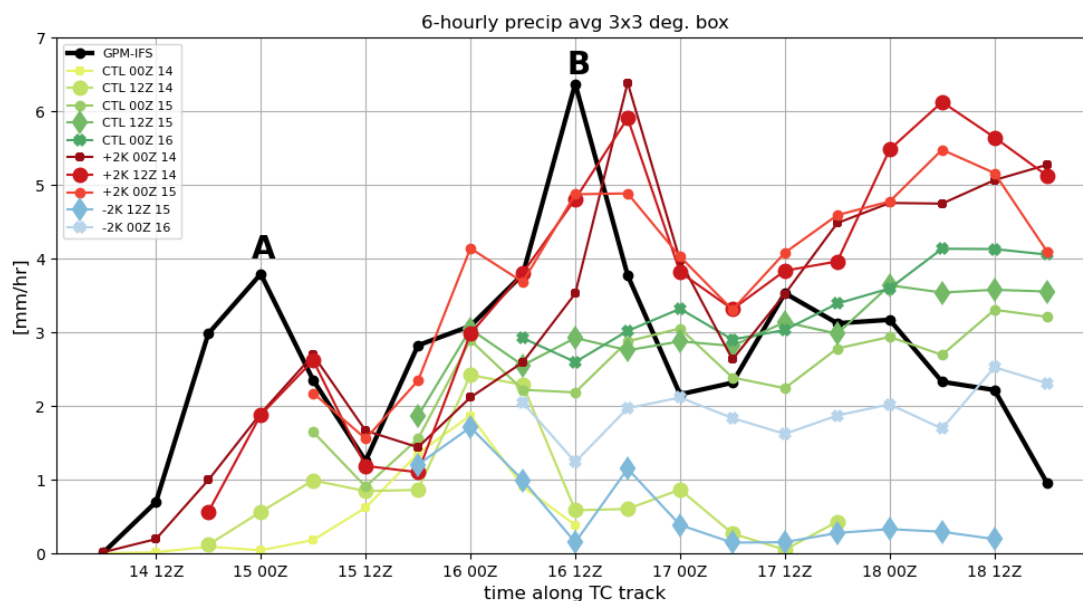


**Figure 6.** Timeseries of 6-hourly precipitation along Ianos’s track, averaged over a  $3 \times 3^\circ$  box with the cyclone at the centre. Same colours and symbols as Fig. 2. A few simulations have been removed for clarity.

Only the simulations with warmer SST, hence stronger surface fluxes leading to enhanced convective activity, are able to simulate the precipitation event before Ianos’s intensification, and one day later the intensification itself. Once the dynamical feedbacks from the preceding precipitation are in the analysis, from 00Z 15 onwards, the simulations with control SST are able to capture Ianos’s intensification as well. However, simulations with -2 K SST initialised on the 15<sup>th</sup> kill the cyclone development. Hence the dynamical feedbacks from the preceding precipitation triggering Ianos’s intensification can be cancelled by weaker surface fluxes. These results highlights the importance of the preceding precipitation event conditioning the environment to become more favourable for Ianos’s intensification.

### 4.3 Evolution of the upper-level structure in the IFS the analysis

An analysis of the upper-level fields, in particular of the PV and the horizontal winds, is performed in this sub-section to explore the baroclinic environment during Ianos’s life time and the preceding precipitation event. Our definition of upper levels is the vertical average between 250 hPa and 200 hPa, the range where the maximum wind speed of the upper-level jet is found.

The IFS analysis at 12Z 14 has a trough extending over the Mediterranean region with stratospheric PV values ( $PV > 2 PVU$ ), shown in Fig. 7.a. Inside the trough, there is a small region of tropospheric PV values ( $PV < 2 PVU$ ) at 15°E, 36°N. This low-PV region could be the result of the blending of tropospheric convective up-drafts generating low-PV values on the



left (and high PV values on the right) of the wind shear vector (Hitchman and Rowe, 2017; Harvey et al., 2020; Oertel et al., 2020). The small surface pressure perturbation that will later develop into medicane Ianos (indicated by the single enclosed of 1010 hPa MSLP contour) sits underneath the jet at 17°E, 32°N. One day later at 12Z 15, immediately after the heavy precipitation event over the Gulf of Sidra (peak “A” in Fig. 5.a), the area of low-valued PV has grown in size and has turned  
285 into a “low-PV bubble” inside the trough (Fig. 7.b). At the surface, Ianos is located at 16°E-33°N on the southern side of the low-PV bubble. With a surface pressure of 1007 hPa it has just begun to intensify, with an emerging cyclonic circulation at low levels (not shown). At 12Z 16, the time of maximum cyclone intensity growth and precipitation around the cyclone, the low-PV bubble has expanded northwards and is associated with a narrow stratospheric PV streamer on its south side, where Ianos is situated (Fig. 7.c). There is a strong southerly flow on the western side of the low-PV bubble, with an anticyclonic curvature  
290 near the cyclone. The irregular shape of the low-PV bubble, with a protuberance of stratospheric PV over the Aegean Sea, suggests that there could be two bubbles merged, a northern one emerging from the preceding precipitation and the southern one from Ianos’s outflow. Twenty four hours later, when the cyclone has reached its TLC form at 12Z 17, the southern branch of the PV streamer cyclonically wraps up around the location of Ianos’s MSLP centre (Fig. 7.d).

Vertical-latitude cross sections through the cyclone at the same times as Fig. 7 are shown in Fig. 8. At 12Z 14 the trough  
295 stretches between 30 and 45°N with southwesterly flow on its southern side and easterly flow on its northern side (Fig. 8.a). The weak pressure perturbation that will later develop into medicane Ianos is located at 32°N and denoted by a dark-blue ‘x’ at the 950 hPa level. At 12Z 15 the tropopause is lifted to the 350 K isentropic level between 33 and 38°N approximately (Fig. 8.b). This feature is the low-PV bubble shown in Fig. 7.b. At the same time the surface signature of Ianos sits underneath the south side of the low-PV bubble at 33°N. There is diabatic activity right above this location, indicated by the vertical filaments of  
300  $PV > 2PVU$ , which are possibly associated with the release of latent heat from the preceding convection event. The vertical-latitude cross section at 12Z 16 shows positive PV production in the vertical at the location of the cyclone at 35°N and negative PV aloft (Fig. 8.c). Convective ascent along the column generates diabatic heating, e.g. via latent heat release, and then the newly generated horizontal gradients of  $\theta$  (magenta contours in Fig. 8.c) produce positive PV, the so-called PV-tower. This PV-tower is a feature of mature cyclones in which low-level positive PV anomalies driven by diabatic processes grow and  
305 align with the PV anomaly associated with upper-level troughs (Čampa and Wernli, 2012). There are another two noteworthy results at this time: (i) the PV streamer south of the cyclone intrudes below 300 hPa and (ii) the southerlies above the PV column, which could be driven by the cyclone’s outflow. At 12Z 17 Ianos completes its tropical-like transition: the positive PV anomaly in the low and mid-levels connects with the upper-level stratospheric intrusion (Fig. 8.d).

A PV streamer cyclonically wrapping up above the cyclone is a common feature of medicanes before its TLC phase  
310 (Homar et al., 2003; Miglietta et al., 2011) and intense Mediterranean cyclones before their maximum intensity (Flaounas et al., 2015, 2021). The PV streamer intrudes into the troposphere reaching lower levels as shown in Fig. 8.c,d and wrapping Ianos on the 335K isentropic level as shown in Fig. 6 of Lagouvardos et al. (2022). The novelty in the results presented here is that the location and width of the PV streamer is heavily influenced by the development of a “low-PV bubble”, which emerges inside the trough after the preceding convective events.

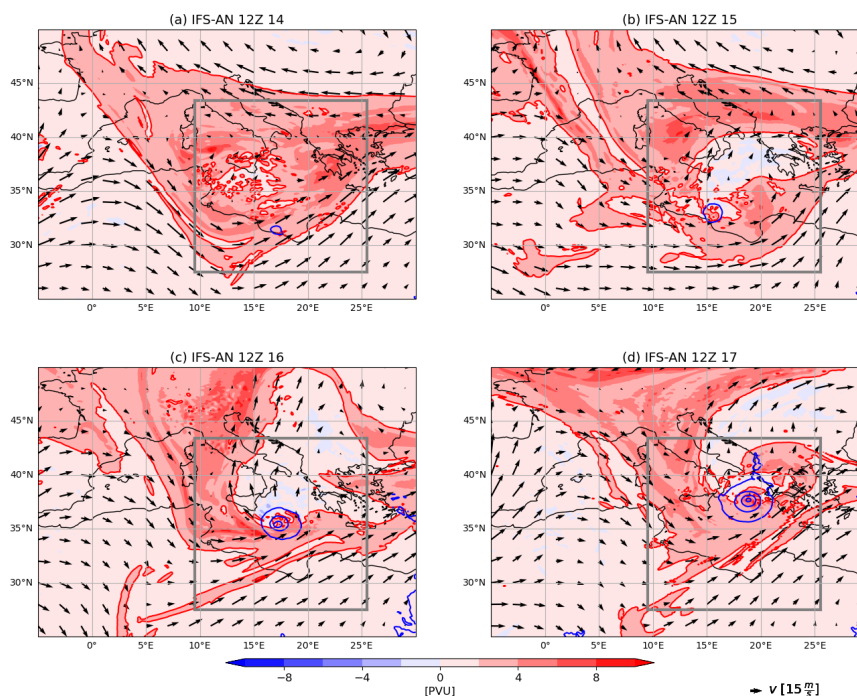


**Figure 7.** IFS analysis PV (colours) and winds (vectors) averaged between 250 hPa and 200 hPa, MSLP (dark-blue contours from 1010 hPa downwards every 5 hPa) at different times: (a) 12Z 14, (b) 12Z 15, (c) 12Z 16, and (d) 12Z 17. Red line indicates the dynamical tropopause contour at  $PV = 2 PVU$ , where  $1 PVU = 10^{-6} Kkg^{-1}m^2s^{-1}$ , Grey box denotes the region where the MetUM simulations are evaluated.

#### 315 4.4 Upper-level structure in the MetUM simulations

The location and timing of the low-PV bubble and the PV streamer on its south side condition the baroclinic environment where medicane Ianos intensifies. Our family of MetUM simulations are well suited to explore this environment. The simulations with earlier initialisation times allow the dynamical features in the upper levels to develop internally in the model, and those with later initialisation times have these dynamical features included in the analysis. Additionally, our simulations with modified  
320 SST overemphasise the effect of enhanced latent heat by stronger surface fluxes (+2 K SST) or reduced diabatic activity with weaker surface fluxes (-2 K SST). Here we analyse the simulations at two different validation times: the end of the preceding precipitation at 12Z 15 and one day later, at 12Z 16, the time of the maximum intensification rate of medicane Ianos.

There are notable differences in the upper-level flow at 12Z 15 across the different simulations initialised at 00Z 14 (Fig. 9, see also Fig. 7.b for a comparison with the IFS analysis). The simulation with 2 K warmer SST shows a wider low-PV  
325 bubble and a stronger anticyclonic flow on its western side than the IFS analysis (Fig. 9.a). Ianos is already present at this

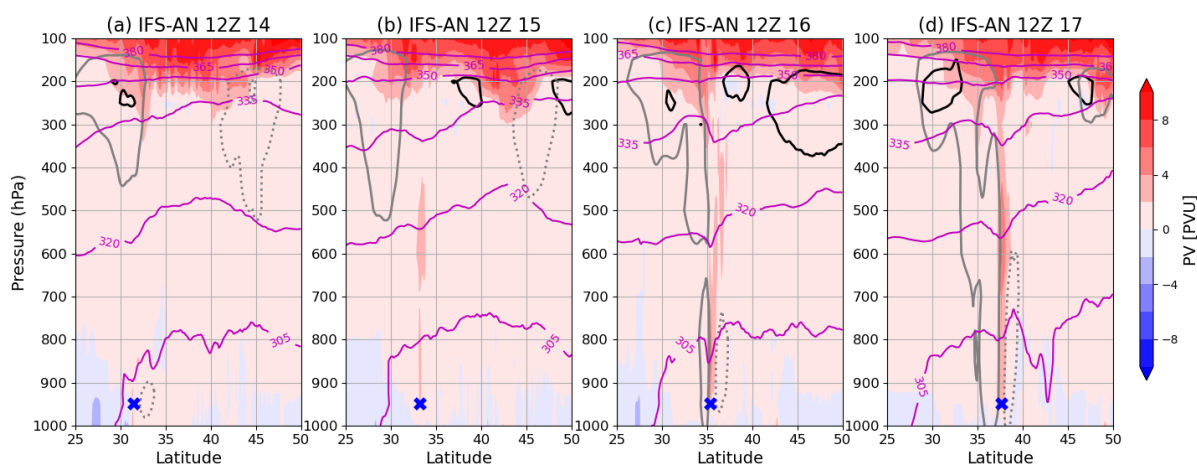


**Figure 8.** Vertical cross sections across latitude for the IFS analysis showing PV (colours),  $\theta$  (magenta contours), meridional winds (black contours with a solid line for southerlies and dashed line for northerlies) and zonal wind (grey contours with a solid line for westerlies and dotted line for easterlies) for different times: (a) 12Z 14, (b) 12Z 15, (c) 12Z 16, and (d) 12Z 17 (same time-layout as Fig. 7). Wind contours are at 15 m/s. The dark-blue cross at 950 hPa denotes the latitude of the cyclone at the time. The location of the cross sections are taken at the longitude of the cyclone and they are longitudinally averaged between  $1^\circ$  west and east of the cyclone longitude.

time in the simulation as a moderately deep cyclone of 1000 hPa (as opposed to a shallow minimum at 1007 hPa in the IFS analysis), and it is located beneath the low-PV bubble at  $33^\circ\text{E}$ ,  $14^\circ\text{N}$ . The simulation with control SST shows an emerging low-PV bubble which has not fully coalesced into a single entity of near-zero PV as in the analysis (Fig. 9.b). It has a more zonal flow around the low-PV pockets. The simulation with  $-2\text{ K}$  SST has a marginal low-PV bubble with no impact on the cyclonic flow (Fig. 9.c). There is a clear influence of surface fluxes enhancing diabatic activity and fostering the development of the low-PV bubble on the simulation with  $+2\text{ K}$  SST, and suppressing its development with  $-2\text{ K}$  SST. The simulation with  $+2\text{ K}$  SST is the closest to the analysis of the three in Fig. 9, despite the strength of Ianos and extent of the low-PV bubble.

From the three simulations initialised at 00Z 14, only the one with  $+2\text{ K}$  SST develops medicane Ianos. It is also the only one of the three showing a wide low-PV bubble with an intensifying Ianos on its south side a day later at 12Z 16 (Fig. 10.a). The anticyclonic curvature of the southerly flow on the west-side of the low-PV bubble is clearer than in the IFS analysis (Fig. 7.c), but less marked than one day earlier in the same simulation (Fig. 9.a). The simulation with control SST shows no Ianos at 12Z 16. This simulation has a weak low-PV bubble that is further downstream and has no anticyclonic southerlies (Fig. 10.b). There is no low-PV bubble, Ianos or anticyclonic southerlies in the simulation with  $-2\text{ K}$  SST (Fig. 10.c).

All the simulations with  $+2\text{ K}$  SST show a broadly similar flow at 12Z 16, with a low-PV bubble, a PV streamer on its south-side, where Ianos is situated while intensifying at this maximum rate, and anticyclonic southerlies on the north-west side of the cyclone (Fig. 10.a,d,g,j,m). Simulations with the three earliest initialisation times show stronger features, e.g., deeper



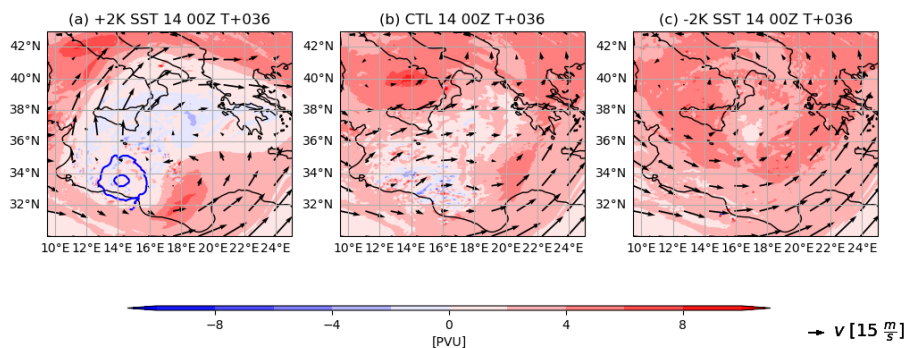


**Figure 9.** Upper-level fields as shown in Fig. 7 for a validation time of 12Z 15 and for MetUM simulations initialised at 00Z 14 for the (a) +2 K SST, (b) control SST and (c) -2 K SST simulations.

cyclones (copper lines with pluses, small-dots and large-dots in Fig. 2) and a wider low-PV bubble with higher curvature of the anticyclonic southerly flow (e.g. going west of Sicily in Fig. 10.a,d,g). The earliest two simulations with -2 K SST do not develop a low-PV bubble (Fig. 10.c,f). The next two develop a low-PV bubble, but it is either small (Fig. 10.i) or further  
345 downstream of a weak Ianos of 1008 hPa (Fig. 10.l). Only the simulation initialised at the latest time captures the cyclone intensification, albeit weaker (Fig. 10.o). This simulation also shows the anticyclonic southerlies on the northwest sector of the cyclone at 15°E, 37°N.

The experiments with control SST at the five different initialisation times have two clear-cut groups. The first group contains the simulations initialised at the latest three times that are able to develop medicane Ianos. These simulations show an  
350 anticyclonic flow emerging from the northwest side of the cyclone (Fig. 10.h,k,n), albeit with a smaller curvature than the equivalent +2 K SST simulations (e.g., Fig. 10.g and 10.h). The second group of simulations with control SST is composed on the simulations initialised at the two earliest times, in which Ianos either does not exist (Fig. 10.b) or does not intensify and remains as a weak surface low of 1010 hPa upstream of the low-PV bubble (Fig. 10.e). Those simulations are unable to develop  
355 Ianos, but they do produce low-PV bubbles. In fact the low-PV bubble shape is very similar between the last simulation unable to develop Ianos, initialised at 12Z 14 (Fig. 10.e) and the first simulation able to develop it, initialised at 00Z 15 (Fig. 10.h). The only perceptible difference is the anticyclonic flow and negative PV on the northwest sector of the cyclone at 16°E, 36°N in the simulation initialised at 00Z 15. Despite these small differences in the upper-level flow, Ianos in the former simulation is a weak surface low of 1010 hPa lagging upstream of the low-PV bubble, whereas Ianos in the later simulation is anchored on the southern side of the bubble and has already deepened below 1000 hPa.

360 The simulations with +2K SST initialised at the earliest two initialisation times are closer to the IFS analysis than the control equivalents. However, for the simulations initialised at 00Z 15 the simulation with control SST is slightly better than

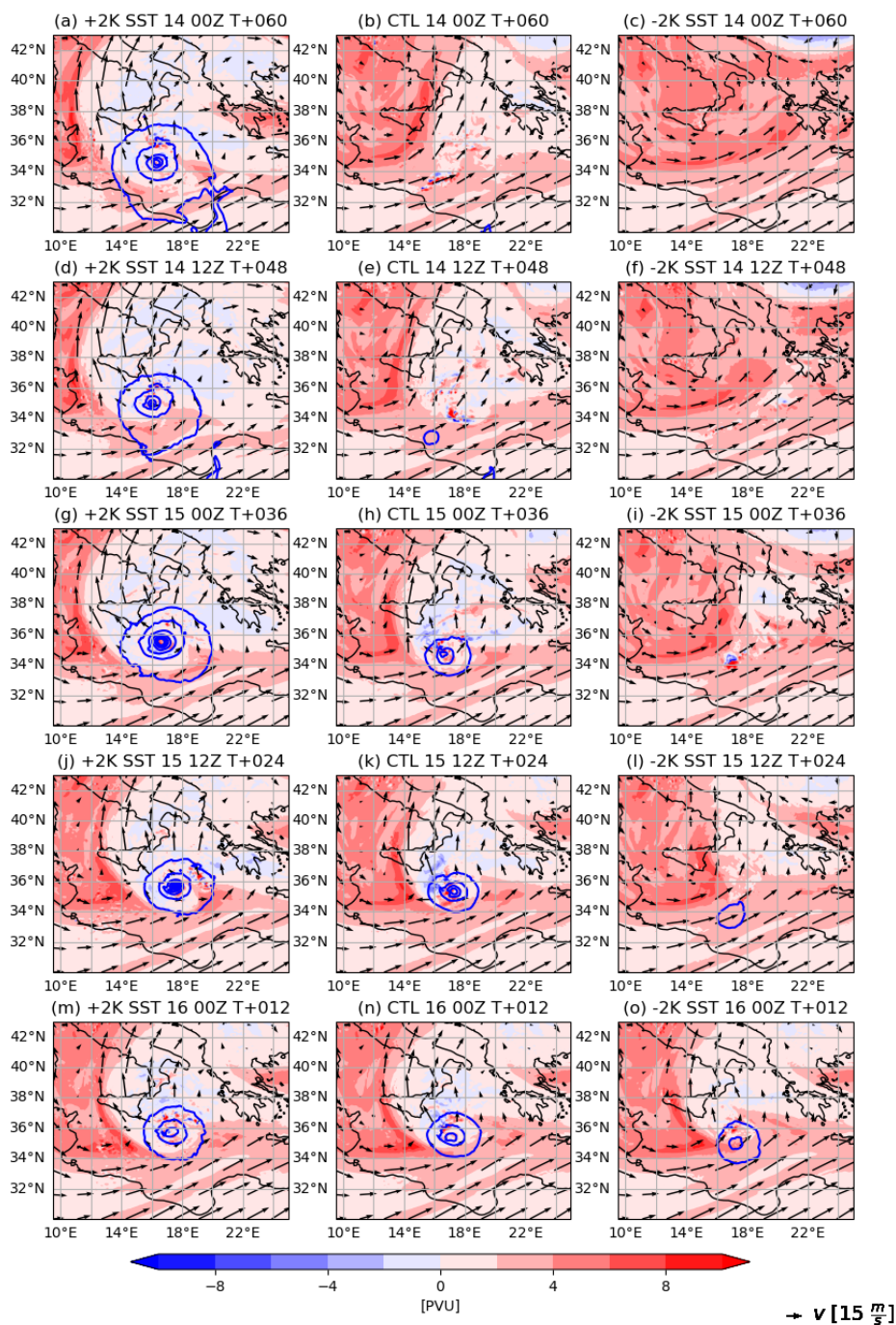


**Figure 10.** Upper-level fields as shown in Fig. 7 for a validation time of 12Z 16 and MetUM simulations initialised at (a,b,c) 00Z 14, (d,e,f) 12Z 14, (g,h,i) 00Z 15, (j,k,l) 12Z 15 and (m,n,o) 00Z 16; with (a,d,g,j,m) +2 K SST, (b,e,h,k,n) control and (c,f,i,l,o) -2 K SST.



the one with +2K SST, as the low-PV bubble in the latter is too wide. For latter two initialisation times, the low-PV bubbles are comparable to the one in the IFS-analysis in the simulations with control and +2K SST. The analysis of the upper-level dynamics reveals three different features in the simulations able to develop medicane Ianos: (i) preceding convection leading to the emergence of a low-PV bubble embedded in a trough, (ii) Ianos's cyclogenesis underneath the southern side of the low-PV bubble, and (iii) strong southerly flow west of the bubble with an anticyclonic curvature north-west of Ianos. The following two sections explore the role of mid-level diabatic processes and upper-level baroclinic forcing on the three features.

#### 4.5 Diabatic forcing of the evolution of the upper-tropospheric structure

The diabatic processes in our case are mostly associated with convection occurring during the preceding precipitation event between late on the 14<sup>th</sup> and early on the 15<sup>th</sup> September, as well as during the intensification of Ianos a day later: peaks "A" and "B" in Fig. 6. The impact of diabatic processes on the upper-level features can be explored with the SGT inversion tool, which can determine the balanced circulation induced by the diabatic heating at any particular time of the simulation. The inversion tool integrates the SGT system described in 2.2 with the MetUM dynamical prognostics (e.g. winds, potential temperature, humidity), and the diabatic tendencies from MetUM physical parametrizations, summed up in the  $S_\theta$  factor (in the second term on the right-hand-side of eq. 1).

To evaluate the ability of the SGT inversion tool to capture the flow and decompose it in diabatic and geostrophically forced parts, we first focus on one event before considering how the diabatic induced flow evolves throughout all three SST experiments. The case is a strong convective event prior to Ianos's cyclogenesis at 18Z 14 in the simulation with +2 K SST initialized at 00Z 14. This event is part of the preceding precipitation event shown in Fig. 5.b. Strong ascent centred at 35°N, 16°E is located inside the low-PV bubble at upper levels, with anticyclonic upper-level winds on its northwest side (Fig. 11.a). The balanced flow from the SGT inversion shows slightly weaker horizontal and vertical winds (Fig. 11.b), and the flow inside the low-PV bubble is more divergent than anticyclonic. These differences can be attributed to the unbalanced flow associated with small-scale processes.

The ageostrophic flow, part of the SGT balanced solution, is markedly divergent around the ascent inside the low-PV bubble (Fig. 12.a), and absent or unorganised elsewhere. Hence, the predominantly anticyclonic upper-level flow surrounding the bubble shown in Fig. 11.b is geostrophic and thus the result of geostrophic adjustment from the temperature gradient between the tropospheric warm air inside the low-PV bubble and the cold stratospheric air outside. There is no ascent nor divergence when diabatic contribution is neglected in the SGT inversion: the *NO – HEAT* solution where  $S_\theta = 0$  (Fig. 12.b). The SGT inverted flow with the diabatic forcing term active and the geostrophic one neglected, the *HEAT – ONLY* solution, produces a very similar ascent and divergent inside the low-PV bubble to the full solution with both terms (Fig. 12.a,c). Hence, the divergent ageostrophic flow inside the low-PV bubble is mostly driven by the diabatic heating. The divergent flow is ageostrophic by definition, so it is discussed without the ageostrophic adjective hereafter.

The vertical-latitude section of the ageostrophic flow averaged between 15.5° and 18.5°E for this convective event preceding Ianos's development is shown in Fig. 13.a. There is strong ascent across the vertical, peaking in the mid levels (~500 hPa). The convective plume induces convergence at lower levels and divergence at upper levels. The SGT inversion without the

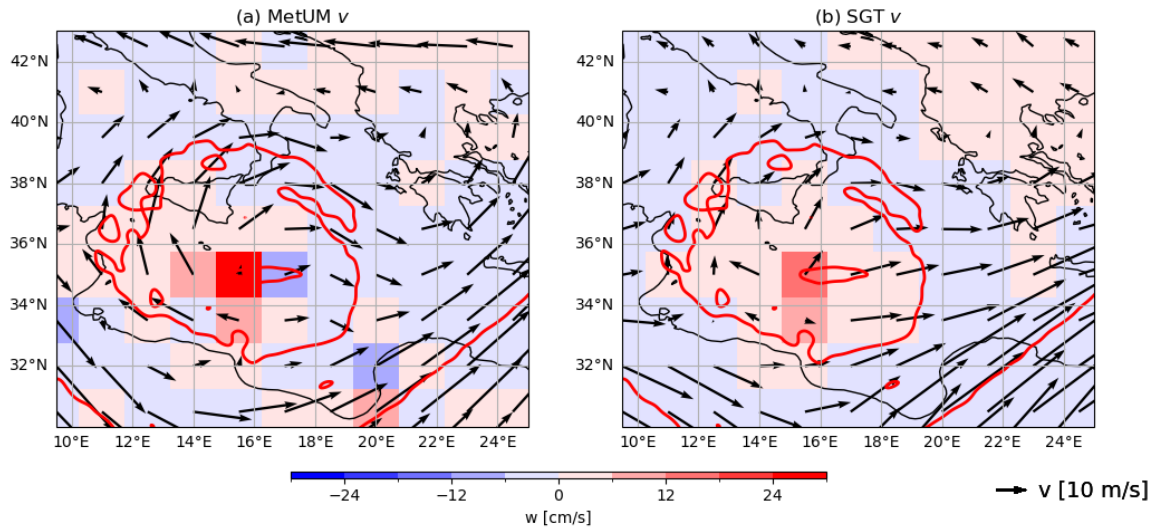


**Figure 11.** Vertical velocity (colours) and horizontal winds (vectors) for the simulation with +2 K SST initialised at 00Z 14 at  $T + 18$ , spectrally filtered to  $0.32^\circ$  and regridded to  $1.5^\circ$ , and vertically averaged between model level 54 (at 10.3 km) and 58 (12.6 km) which is roughly equivalent to the 200 and 250 hPa pressure levels. The red contours shows the spectrally filtered PV from MetUM at 2 PVU ( $< 2$  PVU within contours): (a) MetUM winds, (b) full winds from the SGT inversion tool

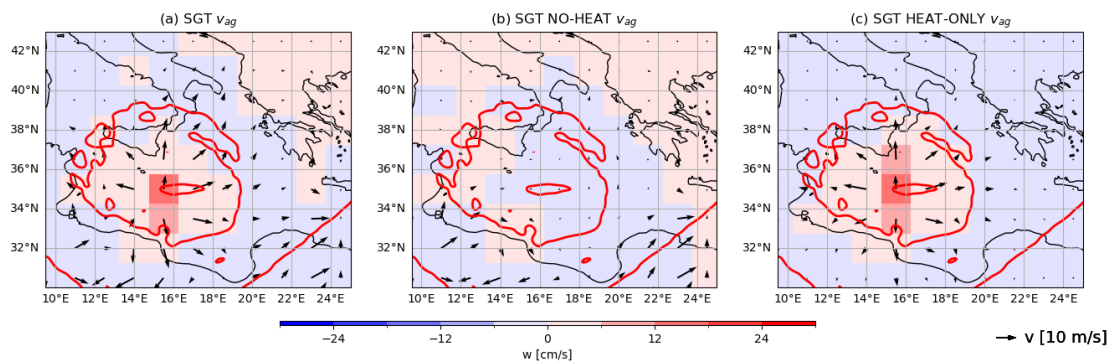


**Figure 12.** Same as Fig. 11 but for the ageostrophic wind inverted from the SGT using (a) full solution with both geostrophic and diabatic forcing terms, (b) SGT inverted flow without heating and (c) SGT inverted flow with only heating. See text for details.

heating contribution shows no ascent nor divergence (Fig. 13.b), and the inversion with only the diabatic forcing active shows



a similar field to the full solution (Fig. 13.a,c). The tropopause elevation on the southward side of the plume is collocated with the divergence contours, highlighting the importance of the diabatic outflow in pushing the tropopause upwards and sideways. In addition to the case described here, vertical ascent induced by diabatic heating and subsequent production of divergence in the upper-levels occurs at other times and simulations. These cases are termed “diabatic divergence” or “diabatic outflow” cases hereafter.

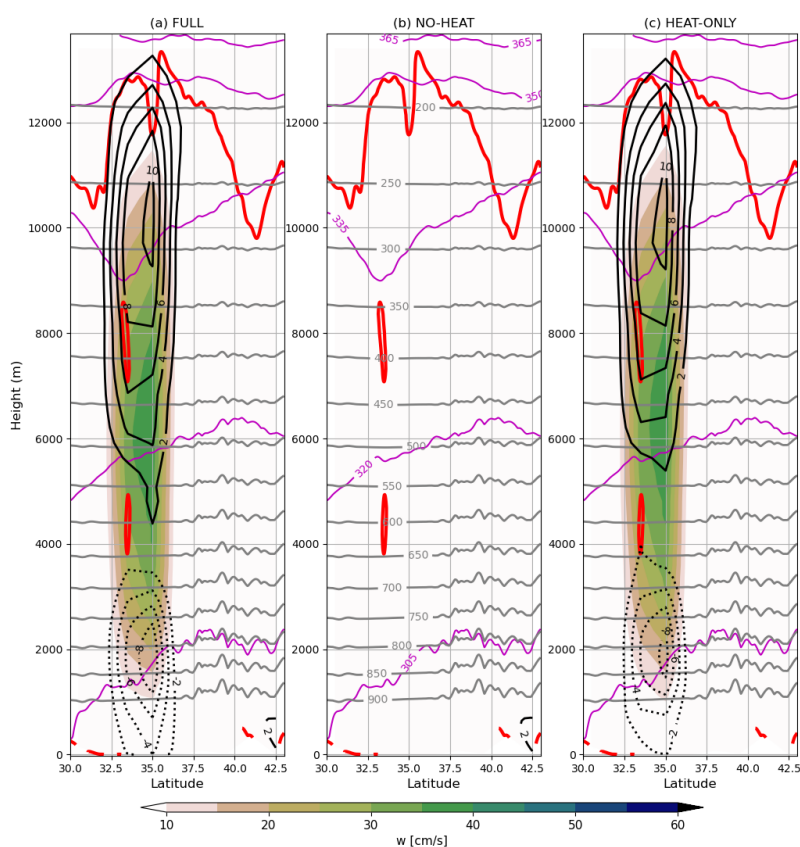


**Figure 13.** Latitudinal cross section for the same case as in Fig. 12 of SGT ageostrophic flow for (a) full solution with both geostrophic and diabatic forcing terms, (b) SGT inverted flow without heating and (c) SGT inverted flow with only heating. Positive values of vertical velocity is shown in colours, divergence in black contours (spaced every  $2 \cdot 10^{-5} \cdot s^{-1}$  from  $2 \cdot 10^{-5} \cdot s^{-1}$ ) and convergence in black dotted contours (analogous values to divergence but negative). MetUM  $\theta$  is shown in magenta contours (spaced every 15 K from 305 K), pressure in grey contours (every 50 hPa from 200 hPa) and PV at 2 PVU (red contour), all spectrally filtered to  $0.32^\circ$ . Labels for  $\theta$  and pressure are only shown in (b) for clarity.



The time evolution of the diabatic outflow and collocation with the low-PV bubble along the cyclone track is shown in Fig. 14, where the  $x$ -axis is the location of the points along the three-hourly cyclone track, and the  $y$ -axis shows the values of diabatic outflow over these locations at other times. The dotted diagonal line denotes when the cyclone transits through each location, with the dots denoting Ianos's MSLP. Thus at a given  $x$ -axis value, times below the dotted line are prior to the arrival of the cyclone at the associated location and times above the dotted line are after its arrival. Similarly, at a given  $y$ -axis value, locations to the left of the line are past track locations and those to the right are future track locations. The locations are defined as the spatial average of a  $3^\circ \times 3^\circ$  box with the cyclone location at the centre. The diabatic divergence is vertically averaged between MetUM levels at roughly 250–300 hPa, and PV between 200–250 hPa, both collocated with their maxima in Fig 13.

The intense diabatic outflow at 18Z 14 in the simulation with +2 K SST initialised at time 00Z 14, shown in Figs. 11-13, is the horizontal line at 18Z 14 between the cyclone's locations  $17^\circ\text{E}$ ,  $32^\circ\text{N}$  and  $36^\circ\text{E}$ ,  $16^\circ\text{N}$  in Fig. 14.a. Its flattened appearance on the diagram is the result of the regridding to  $1.5^\circ$  done by the SGT inversion tool, so a single event may stretch over several points where the cyclone transits. Along with the diabatic outflow, the low-PV bubble (white region within the red contour) emerges at the same time as this intense episode over the locations where the cyclone transits from 18Z 14 until 00Z 17. Once the cyclone is underneath the low-PV bubble at 00Z 15, it begins to intensify with frequent diabatic divergence around it, e.g., at 12Z 15, 06Z 16 and 18Z 16–06Z 17. Neither of the other two simulations initialised at the earliest time (00Z 14) develop medicane Ianos. There is a short-lived low-PV bubble and weak diabatic outflow after 12Z 15 in the simulation with control SST (Fig. 14.b), but neither of these two elements in the simulation with -2 K SST (Fig. 14.c). The set of simulations initialised at 12Z 14 shows similar differences across SST experiments to the ones initialised 12 hours earlier. The simulation with +2 K SST shows the early emergence of the low-PV bubble and it is co-occurring with the intensification of Ianos, but with weaker diabatic outflow at the time of the first precipitation maxima early on the  $15^{\text{th}}$  (Fig. 14.d). The simulation with control SST shows weak diabatic divergence between 18Z 15 and 06Z 16 and between  $17^\circ\text{E}$ ,  $32^\circ\text{N}$  and  $18^\circ\text{E}$ ,  $34^\circ\text{N}$ , and a weak cyclone that never deepens beyond 1008 hPa moving in and out of the low-PV bubble (Fig. 14.e). This association suggests that the low-PV bubble influences the early intensification of the cyclone rather than the other way around. Similarly to the previous simulation with -2 K SST, the simulation initialised at 12Z 14 with -2 K SST has no diabatic outflow and no low-PV bubble (Fig. 14.f).

The simulations with +2 K SST initialised at the three latest times also show strong diabatic outflow inside the low-PV bubble (Fig. 14.g,j,m), with the one initialised at 00Z 15 displaying the highest values. However, although this simulation generates stronger diabatic outflow than the earlier two simulations, it does not develop a deeper Ianos (copper line with small dots versus copper lines with pluses and large dots in Fig. 2). Ianos moves ahead of a high-PV area in the two latest simulations before 00Z 17 but in earlier simulations the high-PV area takes longer to reach the same locations, probably due to the strong outflow pushing the high-PV area away from the cyclone, as shown in Figs. 9.a and 10.a,d,g. The first control simulation to develop an intense Ianos, the one initialised at 00Z 15, is the first to show the surface cyclone travelling underneath the low-PV bubble from the  $15^{\text{th}}$  to  $17^{\text{th}}$  and associated with areas that have episodic diabatic outflow (Fig. 14.h). Ianos travels ahead of a high-PV area, the PV-streamer south of the low-PV bubble shown in Fig 10.h. The simulations with -2 K SST initialised at the latest three times show episodes of diabatic outflow, but these are weak and isolated in the earliest two, initialised at 00Z 15 and

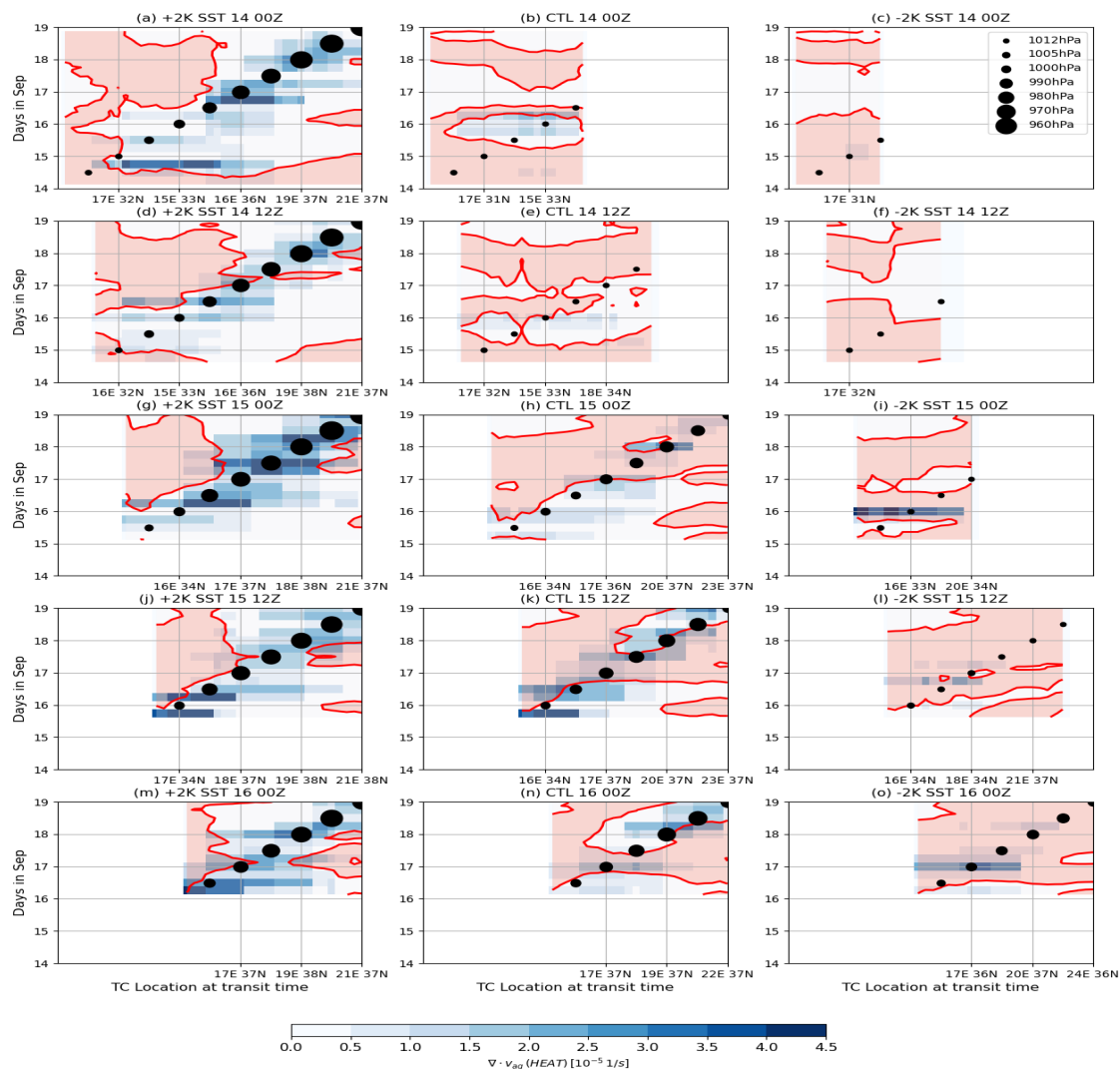


**Figure 14.** Hovmöller of diabatic divergence (colour) vertically averaged between 250–300 hPa, and PV (red shaded for  $PV > 2PVU$ ) between 200–250 hPa. The  $x$ -axis is the location of Ianos at the different points of its trajectory and the  $y$ -axis is time (days in September 2020). See text for further details. dots on the 1:1 line denote the cyclone depth in MSLP every 12 hours, see legend in (c). Simulations initialised at 00Z 14 are (a) +2 K SST, (b) control SST, (c) -2 K SST. Similarly, (d,e,f) for the simulations initialised at 12Z 14, (g,h,i) for 00Z 15, (j,k,l) for 12Z 15 and (m,n,o) for 00Z 16. Only points where the cyclone MSLP is below 1012 hPa are shown.



12Z 15 (Fig. 14.i,l). In contrast, the one initialised at the latest time shows regular diabatic outflow at 06Z 16 and from 18Z 16 to 12Z 17 (Fig. 14.o) and, unlike the earlier two, the low pressure of Ianos is sustained and the cyclone does not weaken with time (blue line with crosses *vs.* blue lines with diamonds and small dots in Fig. 2).

440 In summary, the results from the SGT inversion tool suggest that the diabatic heating produced in the preceding precipitation event late on the 14<sup>th</sup> and early on the 15<sup>th</sup> creates a divergent balanced flow in the upper levels, one of the main contributors (if not the only one) to the development of the low-PV bubble. Simulations missing the right timing of the diabatic outflow and low-PV bubble also miss Ianos's intensification. The diabatic outflow continues while Ianos intensifies, but is located next to a PV streamer on its southern side, in particular on the 15<sup>th</sup>. This is an ideal baroclinic environment for Ianos's evolution. The  
445 contribution of upper-level baroclinicity in the early development of Ianos is explored in the next section.

#### 4.6 Upper-tropospheric baroclinic forcing

The growth of the low-PV bubble, enhanced by diabatic processes, produces height-dependent advection of geostrophic relative vorticity and creates the necessary conditions in the upper levels to force QG ascent, following the VA term in eq. 3 in section 2.3. We explore the QG ascent in two simulations with control SST: one initialised at 12Z 14 in which Ianos does not intensify, which is thus termed the “poor simulation”, and one initialised at 00Z 15 in which Ianos does intensify, termed the “good simulation” (green lines with small and large dots in Fig. 2). Note that these two simulations are contrasted because of the  
450 markedly different cyclone development with only 12 hours difference in the initialisation time. The QG ascent is evaluated at 12Z 15, the time when Ianos starts to intensify under the presence of the low-PV bubble. The height attributable solution of the QG omega equation is obtained when forced by the upper levels (600–100 hPa), or forced by the lower levels (1000–800 hPa).  
455 The QG forced vertical motion is first evaluated at 700 hPa, the typical steering level of baroclinic disturbances and also a level with a clear connection to the near-surface cyclone structure but sufficiently high to avoid boundary layer effects (Deveson et al., 2002). The poor and good simulations both produce very similar QG vertical motions when forced by the lower levels at 12Z 15 (Fig. 15.a,b), with a maximum positive ascent of around 5 mm/s below the low-PV bubble at 16°E, 33°N and a region of subsidence to the southwest at 14°E, 32°N. The peaks are slightly stronger in the good simulation than in the poor one. The  
460 differences amongst the simulations are clearer in the QG vertical motion forced by upper levels, although the values are quite weak, around 2 mm/s. There is ascent at 16°E, 32°N underneath the PV gradient on the southern side of the low-PV bubble and subsidence below the southwest corner of the low-PV bubble at 15°E, 34°N in the good simulation (Fig 15.c). The subsidence is at the southern edge of an area of upper-level high cyclonic vorticity, which moves northeastwards pushed by the background flow. Such positive advection of vorticity in the upper-levels is associated with QG ascent following the VA term in the QG  
465 omega equation. The vertical motion forced by the upper-levels at 700 hPa underneath the low-PV bubble is nearly absent in the poor simulation (Fig 15.d). The upper-level flow in the southern sector of the low-PV bubble is more zonal and thus the vorticity there is smaller, decreasing the VA term. In summary, results from Fig. 15 suggest that Ianos's intensification does not come from low-level forcing, which is very similar in both simulations. Instead, the advection of the upper-level low-PV bubble, and its associated geostrophic vorticity, forces ascent that is stronger in the good simulation.



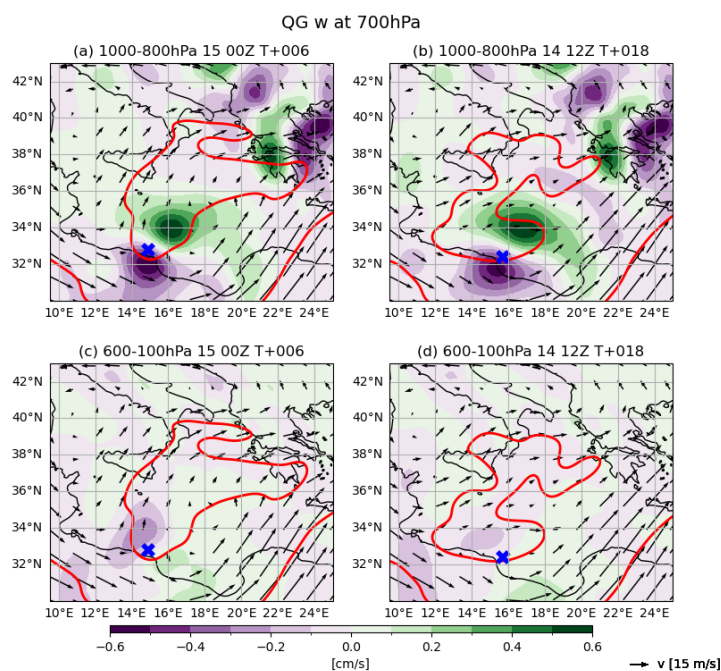


**Figure 15.** QG vertical velocity at 700 hPa and at 12Z 15 forced by (a,b) lower levels (1000–800 hPa) and (c,d) upper levels (600–100 hPa), for simulations with control SST initialised at (a,c) 00Z 15, defined as the “good simulation” in the text, and (b,d) 12Z 14, the “poor simulation”. The red contour shows PV at 2 PVU, and vectors show the horizontal wind, both spectrally filtered to  $1.6^\circ$  and vertically averaged between 250–200 hPa. The blue ‘x’ shows the location of the low-level cyclone that later develops into Ianos in the good simulation.

470 The longitudinal cross section at the cyclone latitude for the QG ascent forced by low levels is shown in Fig. 16a,b with the  $\theta_w$  field overplotted. There is a dipole of subsidence and ascent centred on the cyclone that is stronger in the good simulation (Fig. 16.a). The  $\theta_w$  field is quite similar in the two simulations. Additionally, the vertical gradient of horizontal wind shear over the areas of high  $\theta_w$  horizontal gradient is also very similar between the two simulations (not shown). Hence, following Griffiths et al. (2000), the production of low-level convective instability is roughly equivalent and thus not a primary factor in  
475 the early development of Ianos. The good forecast shows ascent forced by upper levels of around 5 cm/s over the 600–500 hPa vertical range (Fig. 16.c) and the values in the poor forecast are 3-5 times smaller smaller (1 cm/s, Fig. 16.d).

In summary, the generation of the low-PV bubble at upper levels via the preceding convection turns the flow northwards and thus generates positive VA. This VA forces ascent beneath it as seen in the good simulation (initialised at 00Z 15) in which the upper-level forced QG ascent is stronger in the upper and mid troposphere than in the poor simulation (initialised at 12Z 14).  
480 The reason why the VA is weaker in the poor simulation is that this simulation generates misplaced preceding convection that is over the Lybian coast rather than over the Sidra Gulf. This convection leads to a more zonally oriented flow in the low-PV bubble and hence this simulation does not create the necessary baroclinic environment to support Ianos’s intensification

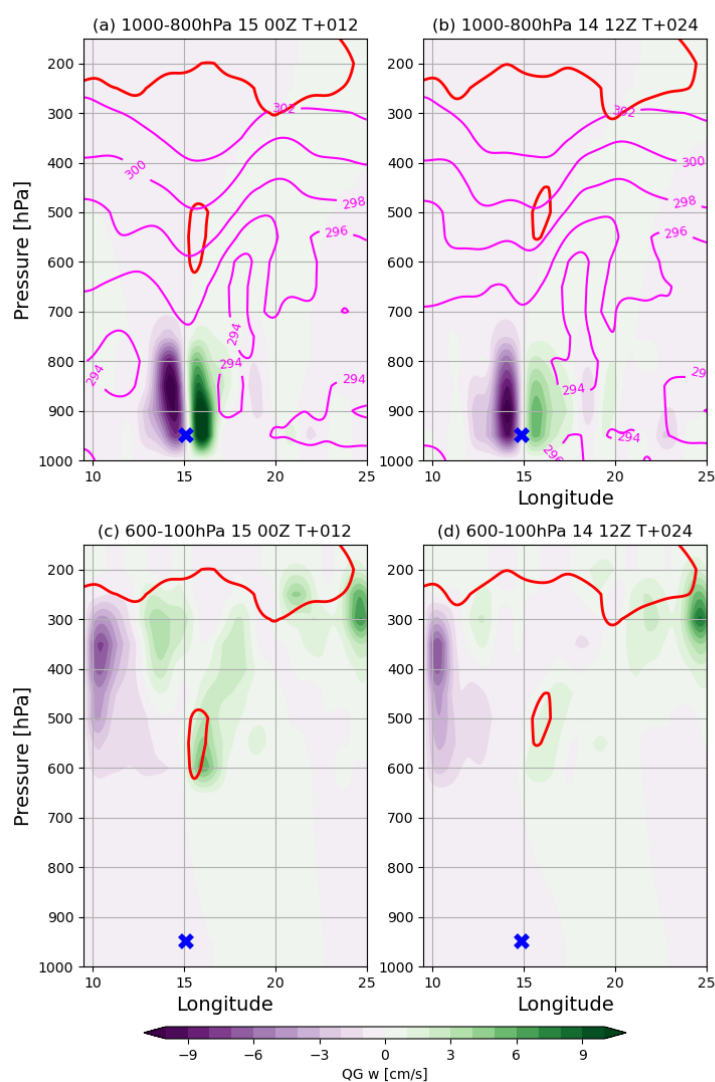


**Figure 16.** Longitudinal cross section of QG vertical velocity (colour) at the cyclone latitude at 12Z 15 following the same layout as Fig. 3. The magenta contours show  $\theta_w$ . Fields are latitudinally averaged between  $0.5^\circ$  west and east. The blue 'x' at 950 hPa marks the location of the surface cyclone. Note, the colour-scale is different to Fig. 15.



## 5 Conclusion

Medicanes are a rare and intense type of cyclones that occur in the Mediterranean region. They show tropical-like features  
485 such as a cloud-less eye and an axisymmetric warm core, uncommon characteristics for their latitude. Their growth is driven  
by a combination of heat fluxes from the sea surface and baroclinic forcing, whose interaction is not yet well-understood. In  
the present study we investigate the predictability and dynamics of medicane Ianos, one of the most intense medicanes ever  
recorded, with convection-permitting MetUM simulations at 2.2 km grid spacing. Ianos's cyclogenesis took place on the 15<sup>th</sup>  
September 2020 over 28°C SST, anomalously 1.5–2 K warmer than climatology, and after intense but unorganised convective  
490 precipitation over the area. It became a tropical-like cyclone after developing an axisymmetric warm core and a cloud-less  
eye early on the 17<sup>th</sup>, making landfall a day later, on the 18<sup>th</sup>, over the Ionian Islands, western Greece. Afterwards it moved  
southwestward, weakened and lost its tropical-like features on the 19<sup>th</sup>. Our simulations hence start at different initialisation  
times to capture different processes, including the preceding precipitation and the rapid intensification prior to Ianos's tropical  
transition. The SST is homogeneously perturbed from the operational OSTIA analysis by +2 K or -2 K to explore the role of  
495 stronger and weaker surface fluxes on Ianos's intensification.

All the simulations with +2 K SST, regardless of the initialisation time, develop a very strong medicane Ianos (some reach  
a minimum MSLP of 950 hPa). The simulations with control SST develop a medicane only in simulations initialised at or  
after 00Z 15. There is only one simulation with -2 K SST that develops a medicane, albeit a weak one, which is the one  
initialised at the latest time (00Z 16). All of the other simulations with -2 K SST fail to fully develop Ianos. Hence, medicane  
500 Ianos might not have existed if SST anomalies in mid-September 2020 were marginal or negative. There is a strong preceding  
precipitation event on the 14<sup>th</sup> and early 15<sup>th</sup>, ahead of Ianos's cyclogenesis, and over regions where the cyclone later transits  
and intensifies. This event is only captured in simulations with warmer SST. Note that the improvement of the simulation  
with warmer SST does not necessarily imply that there is an error in the simulated surface fluxes in the control simulation.  
Instead, the enhanced fluxes may be compensating for one or more missing or poorly parametrized processes in the MetUM  
505 with RAL2M configuration. There is also a second precipitation maxima, occurring around the cyclone at 12Z 16, when it is  
intensifying at its maximum rate. The second precipitation peak has been shown to occur in other medicanes (Fita and Flaounas,  
2018; Miglietta et al., 2013), but the preceding precipitation event about three days before the peak in medicane intensity has  
not previously been associated with medicane cyclogenesis to the authors' knowledge.

Under a baroclinic framework Mediterranean cyclones intensify from a stratospheric intrusion generating the necessary PV  
510 gradients in the upper troposphere (Flaounas et al., 2015, 2021). In the case of Ianos, the picture is similar but the origin of the  
PV gradients is unusual. The stratospheric intrusion, associated to a homogeneous positive PV anomaly, overshadows the area  
where Ianos intensifies and, during the preceding precipitation, tropospheric low-PV pockets are deposited aloft that coalesce  
into a single entity, termed a low-PV bubble here, within the stratospheric intrusion.

The inverted semi-geostrophic flow from the MetUM simulations during the preceding precipitation event shows ascent with  
515 divergent outflow in the upper levels that is fully attributable to diabatic heating produced by MetUM physical parametriza-  
tions. The divergent outflow pushes the tropopause upwards and sideways and either drives or substantially contributes to the



development of the low-PV bubble. In those simulations developing a medicane Ianos there is also diabatic outflow later on during the 16<sup>th</sup> when Ianos intensifies at the highest rate, and also while it attains tropical-like features. The low-PV bubble is associated with geostrophic vorticity in the upper levels on the 15<sup>th</sup>, the advection of which activates the baroclinic development of a surface low beneath it and coming from the Libyan coast. The upper-level baroclinic forcing is insufficient to generate strong cyclogenesis by itself as evidenced by the simulations with -2 K SST.

The processes for Ianos's intensification drawn from the analysis of our simulations can be summarised in three steps:

1. The preceding precipitation event deposits or creates low-valued PV in the upper troposphere late on the 14<sup>th</sup> and early on the 15<sup>th</sup>, forming a low-PV bubble inside the trough. Diabatic heating released by convective ascent induces a balanced divergent flow in the upper levels that contributes to the low-PV bubble formation and growth.
2. The geostrophic adjustment from the low-PV bubble is associated with geostrophic vorticity around the bubble as it expands early on the 15<sup>th</sup>. The upper-level forcing from the vertical gradient of the advection of the geostrophic vorticity is associated with quasi-geostrophic ascent, which favours Ianos's cyclogenesis on the 15<sup>th</sup>.
3. During Ianos's intense growth on the 16<sup>th</sup>, a PV tower is formed at its centre and the upper-level flow on its northwest sector turns anticyclonic. There is also divergent diabatic outflow aloft signalling the strength of diabatic processes producing positive PV in the column.

The simulations that follow steps 1 and 2 and develop medicane Ianos either have (a) +2 K SST enabling them to simulate the emergence of the low-PV bubble after the preceding precipitation events or (b) control SST but were initialised at a later time, once the analysis contains the low-PV bubble and associated geostrophic vorticity over the right locations. For the simulations with -2 K SST, only the one initialised at the latest time follows step 3 above, and thus is able to sustain Ianos's intensification. All the other ones are initialised during or before Ianos's cyclogenesis and hence they cannot draw enough energy from surface fluxes to sustain the diabatic activity in the PV tower and the associated divergent diabatic outflow at upper levels.

Although identified here during medicane development for the first time, preceding or preconditioning precipitation events are common in the extra-tropical transition of tropical cyclones. The cyclones advect warm and moist air poleward, triggering extratropical cyclogenesis and initiating ridge building and jet acceleration ahead of the tropical cyclones (Grams and Archambault, 2016). Similarly, preceding precipitation has an important role in the formation of tropical cyclones from extratropical precursors. Upper-tropospheric outflow from convection reduces vertical shear which, when it is located upshear from a surface low, favours tropical transition and triggers the WISHE mechanism (Davis and Bosart, 2004), a processes detailed for hurricane Michael in Davis and Bosart (2003).

The combination of diabatic divergence with anticyclonic balanced motion around the cyclone is also a characteristic of the extra-tropical transition of tropical cyclones. In these cyclones the flow can be decomposed into a (i) cyclonic circulation around the cyclone's PV tower, (ii) balanced anticyclonic circulation associated with the anticyclonic PV anomaly of the upper-tropospheric outflow, and (iii) the upper-tropospheric divergent outflow associated with latent heat release below (Figure 3 in Keller et al. 2019). Our results show that the diabatic divergent outflow helps to create the vorticity gradients and hence quasi-geostrophic forced ascent, creating a feedback between diabatic processes induced by surface fluxes, and baroclinic forcing

in the upper levels. The upper-level balanced cyclonic circulation around the cyclone described in Keller et al. (2019) is not present until Ianos has fully developed its tropical-like features, and hence makes a marginal contribution to its development.

We make the following recommendations for model development from our findings. The representation of convective processes in the preceding precipitation event in the simulations with control SST is poor. Either finer resolutions or better physics  
555 such as a scale aware convection scheme or a two moment cloud scheme for example might improve the simulation of these processes and hence the predictability of cyclones such as medicane Ianos. Additionally, capturing SST evolution is important for medicane prediction, either by coupling to ocean models as done in Ricchi et al. (2017) and Stathopoulos et al. (2020), or updating SST from an operational ocean-only system (Mahmood et al., 2021). The global methodologies to perturb SST in the ensemble system such as the one described in Tennant and Beare (2014), with amplitudes as large as 2 K, may be needed to  
560 coarsely represent the uncertainty around medicane intensification.

The simulations with +2 K SST have provided insightful results to interpret the intensification mechanisms, but also a terrifying vision of a 950 hPa cyclone over the Mediterranean (Fig. 4.a). The strength of the medicane in our simulations with +2 SST may be excessive as the near-surface atmospheric temperatures were not adjusted and SST were fixed, thus cooling  
565 feedbacks between atmosphere and ocean not represented. However, given the relationship between SST and medicane strength found here and elsewhere, e.g. Miglietta et al. (2011) and Noyelle et al. (2019), quantifying SST changes with climate change, and their uncertainties, is critical to determining the future climatology of medicanes.

*Code availability.* MetUM model is available for use under a closed licence agreement, further information at <http://www.metoffice.gov.uk/research/modelling-systems/unified-model> (last access: 19 October 2023). The SGT inversion tool is available at the MetOffice Science Repository Service (MOSRS) at <https://code.metoffice.gov.uk/svn/utills/sgdiagnostic/> (last access: 19 October 2023)

570 *Data availability.* MetUM simulations are archived in Met Office Operational Storage Environment (MOOSE) at devfc/u-ci649 (control SST), devfc/u-cl004 (+2K SST) and devfc/u-cl005 (-2K SST), available upon request. IFS analysis are available at the ECMWF's Meteorological Archive Retrieval System (MARS) Catalogue

*Author contributions.* **CS** led the simulations, data analysis, visualization and writing. **SG** provided the Quasi-Geostrophic diagnostics and contributed substantially to conceptualisation and writing. **AV** contributed to conceptualisation and writing. **FP** and **SD** designed the model  
575 protocol for the simulations and contributed to writing. **SB** contributed to the conceptualisation and writing.

*Competing interests.* Co-author Silvio Daviolo is a member of the editorial board of WCD.



*Acknowledgements.* This article is based upon work from COST Action CA19109 "MedCyclones", supported by COST (European Cooperation in Science and Technology). Authors would like to thank Emanuele Gentile, Julian Hemming and John Methven for their scientific and technical advice.



## 580 References

- Abel, S. J. and Boutle, I. A.: An improved representation of the raindrop size distribution for single-moment microphysics schemes, *Quart. J. Roy. Meteorol. Soc.*, 138, 2151–2162, <https://doi.org/10.1002/qj.1949>, 2012.
- Beare, R. J. and Cullen, M. J. P.: A semi-geostrophic model incorporating well-mixed boundary layers, *Quart. J. Roy. Meteorol. Soc.*, 136, 906–917, <https://doi.org/10.1002/qj.612>, 2010.
- 585 Best, M. J., Pryor, M., Clark, D. B., Rooney, G. G., Essery, R. L. H., Ménard, C. B., Edwards, J. M., Hendry, M. A., Porson, A., Gedney, N., Mercado, L. M., Sitch, S., Blyth, E., Boucher, O., Cox, P. M., Grimmond, C. S. B., and Harding, R. J.: The Joint UK Land Environment Simulator (JULES), model description – Part 1: Energy and water fluxes, *Geosci. Model Dev.*, 4, 677–699, <https://doi.org/10.5194/gmd-4-677-2011>, 2011.
- Boutle, I. A. and Morcrette, C. J.: Parametrization of area cloud fraction, *Atm. Sci. Lett.*, 11, 283–289, <https://doi.org/10.1002/asl.293>, 2010.
- 590 Boutle, I. A., Eyre, J. E. J., and Lock, A. P.: Seamless Stratocumulus Simulation across the Turbulent Gray Zone, *Mon. Weather Rev.*, 142, 1655 – 1668, <https://doi.org/10.1175/MWR-D-13-00229.1>, 2014.
- Brown, A., Milton, S., Cullen, M., Golding, B., Mitchell, J., and Shelly, A.: Unified Modeling and Prediction of Weather and Climate: A 25-Year Journey, *Bull. Amer. Meteorol. Soc.*, 93, 1865 – 1877, <https://doi.org/10.1175/BAMS-D-12-00018.1>, 2012.
- Bush, M., Boutle, I., Edwards, J., Finnenkoetter, A., Franklin, C., Hanley, K., Jayakumar, A., Lewis, H., Lock, A., Mittermaier, M., Mohandas, S., North, R., Porson, A., Roux, B., Webster, S., and Weeks, M.: The second Met Office Unified Model–JULES Regional Atmosphere and Land configuration, RAL2, *Geosci. Model Dev.*, 16, 1713–1734, <https://doi.org/10.5194/gmd-16-1713-2023>, 2023.
- 595 Carrió, D., Homar, V., Jansa, A., Romero, R., and Picornell, M.: Tropicalization process of the 7 November 2014 Mediterranean cyclone: Numerical sensitivity study, *Atmos. Res.*, 197, 300–312, <https://doi.org/10.1016/j.atmosres.2017.07.018>, 2017.
- Castillo, J. M., Lewis, H. W., Mishra, A., Mitra, A., Polton, J., Brereton, A., Saulter, A., Arnold, A., Berthou, S., Clark, D., Crook, J., Das, A., Edwards, J., Feng, X., Gupta, A., Joseph, S., Klingaman, N., Momin, I., Pequignet, C., Sanchez, C., Saxby, J., and Valdivieso da Costa, M.: The Regional Coupled Suite (RCS-IND1): application of a flexible regional coupled modelling framework to the Indian region at kilometre scale, *Geosci. Model Dev.*, 15, 4193–4223, <https://doi.org/10.5194/gmd-15-4193-2022>, 2022.
- 600 Cavicchia, L., von Storch, H., and Gualdi, S.: A long-term climatology of medicanes, *Clim. Dynam.*, 43, 1183–1195, <https://doi.org/10.1007/s00382-013-1893-7>, 2014.
- 605 Cioni, G., Malguzzi, P., and Buzzi, A.: Thermal structure and dynamical precursor of a Mediterranean tropical-like cyclone, *Quarterly Journal of the Royal Meteorological Society*, 142, 1757–1766, <https://doi.org/10.1002/qj.2773>, 2016.
- Cullen, M.: The Use of Semigeostrophic Theory to Diagnose the Behaviour of an Atmospheric GCM, *Fluids*, 3, <https://doi.org/10.3390/fluids3040072>, 2018.
- Cullen, M. J. P., Douglas, R. J., Roulstone, I., and Sewell, M. J.: Generalized semi-geostrophic theory on a sphere, *J. Fluid Mech.*, 531, 123–157, <https://doi.org/10.1017/S0022112005003812>, 2005.
- 610 Da Silva, N. A., Webber, B. G. M., Matthews, A. J., Feist, M. M., Stein, T. H. M., Holloway, C. E., and Abdullah, M. F. A. B.: Validation of GPM IMERG Extreme Precipitation in the Maritime Continent by Station and Radar Data, *Earth Space Sci.*, 8, e2021EA001738, <https://doi.org/10.1029/2021EA001738>, e2021EA001738 2021EA001738, 2021.
- Davies, H. C.: The Quasigeostrophic Omega Equation: Reappraisal, Refinements, and Relevance, *Mon. Weather Rev.*, 143, 3 – 25, <https://doi.org/10.1175/MWR-D-14-00098.1>, 2015.
- 615



- Davis, C. A. and Bosart, L. F.: Baroclinically Induced Tropical Cyclogenesis, *Mon. Weather Rev.*, 131, 2730 – 2747, [https://doi.org/10.1175/1520-0493\(2003\)131<2730:BITC>2.0.CO;2](https://doi.org/10.1175/1520-0493(2003)131<2730:BITC>2.0.CO;2), 2003.
- Davis, C. A. and Bosart, L. F.: The TT Problem: Forecasting the Tropical Transition of Cyclones, *Bull. Amer. Meteorol. Soc.*, 85, 1657 – 1662, <https://doi.org/10.1175/BAMS-85-11-1657>, 2004.
- 620 Denis, B., Côté, J., and Laprise, R.: Spectral Decomposition of Two-Dimensional Atmospheric Fields on Limited-Area Domains Using the Discrete Cosine Transform (DCT), *Mon. Weather Rev.*, 130, 1812 – 1829, [https://doi.org/10.1175/1520-0493\(2002\)130<1812:SDOTDA>2.0.CO;2](https://doi.org/10.1175/1520-0493(2002)130<1812:SDOTDA>2.0.CO;2), 2002.
- Deveson, A. C. L., Browning, K. A., and Hewson, T. D.: A classification of FASTEX cyclones using a height-attributable quasi-geostrophic vertical-motion diagnostic, *Quart. J. Roy. Meteorol. Soc.*, 128, 93–117, <https://doi.org/10.1256/00359000260498806>, 2002.
- 625 Di Muzio, E., Riemer, M., Fink, A. H., and Maier-Gerber, M.: Assessing the predictability of Medicanes in ECMWF ensemble forecasts using an object-based approach, *Quarterly Journal of the Royal Meteorological Society*, 145, 1202–1217, <https://doi.org/https://doi.org/10.1002/qj.3489>, 2019.
- Diakakis, M., Mavroulis, S., Filis, C., Lozios, S., Vassilakis, E., Naoum, G., Soukis, K., Konsolaki, A., Kotsi, E., Theodorakidou, D., Skourtsos, E., Kranis, H., Gogou, M., Spyrou, N. I., Katsetsiadou, K.-N., and Lekkas, E.: Impacts of Medicanes on Geomorphology and Infrastructure in the Eastern Mediterranean, the Case of Medicane Ianos and the Ionian Islands in Western Greece, *Water*, 15, <https://doi.org/10.3390/w15061026>, 2023.
- 630 Donlon, C. J., Martin, M., Stark, J., Roberts-Jones, J., Fiedler, E., and Wimmer, W.: The Operational Sea Surface Temperature and Sea Ice Analysis (OSTIA) system, *Remote Sens. Environ.*, 116, 140–158, <https://doi.org/10.1016/j.rse.2010.10.017>, 2012.
- ECMWF: Summary of cycle 47r1, <https://www.ecmwf.int/en/forecasts/about-our-forecasts/evolution-ifs/cycles/summary-cycle-47r1>, last  
635 accessed 19-October-2023, 2020.
- Emanuel, K. A.: An Air-Sea Interaction Theory for Tropical Cyclones. Part I: Steady-State Maintenance, *J. Atmos. Sci.*, 43, 585 – 605, [https://doi.org/10.1175/1520-0469\(1986\)043<0585:AASITF>2.0.CO;2](https://doi.org/10.1175/1520-0469(1986)043<0585:AASITF>2.0.CO;2), 1986.
- Ferrarin, C., Pantillon, F., Davolio, S., Bajo, M., Miglietta, M. M., Avolio, E., Carrió, D. S., Pytharoulis, I., Sanchez, C., Patlakas, P., González-Alemán, J. J., and Flaounas, E.: Assessing the coastal hazard of Medicane Ianos through ensemble modelling, *Nat. Hazards Earth Syst. Sci.*, 23, 2273–2287, <https://doi.org/10.5194/nhess-23-2273-2023>, 2023.
- 640 Fita, L. and Flaounas, E.: Medicanes as subtropical cyclones: the December 2005 case from the perspective of surface pressure tendency diagnostics and atmospheric water budget, *Quart. J. Roy. Meteorol. Soc.*, 144, 1028–1044, <https://doi.org/10.1002/qj.3273>, 2018.
- Flaounas, E., Raveh-Rubin, S., Wernli, H., Drobinski, P., and Bastin, S.: The dynamical structure of intense Mediterranean cyclones, *Clim. Dynam.*, 44, 2411–2427, <https://doi.org/10.1007/s00382-014-2330-2>, 2015.
- 645 Flaounas, E., Gray, S. L., and Teubler, F.: A process-based anatomy of Mediterranean cyclones: from baroclinic lows to tropical-like systems, *Weather Clim. Dynam.*, 2, 255–279, <https://doi.org/10.5194/wcd-2-255-2021>, 2021.
- Flaounas, E., Davolio, S., Raveh-Rubin, S., Pantillon, F., Miglietta, M. M., Gaertner, M. A., Hatzaki, M., Homar, V., Khodayar, S., Korres, G., Kotroni, V., Kushta, J., Reale, M., and Ricard, D.: Mediterranean cyclones: current knowledge and open questions on dynamics, prediction, climatology and impacts, *Weather Clim. Dynam.*, 3, 173–208, <https://doi.org/10.5194/wcd-3-173-2022>, 2022.
- 650 Giorgi, F.: Climate change hot-spots, *Geophys. Res. Lett.*, 33, <https://doi.org/10.1029/2006GL025734>, 2006.
- Grams, C. M. and Archambault, H. M.: The Key Role of Diabatic Outflow in Amplifying the Midlatitude Flow: A Representative Case Study of Weather Systems Surrounding Western North Pacific Extratropical Transition, *Mon. Weather Rev.*, 144, 3847 – 3869, <https://doi.org/10.1175/MWR-D-15-0419.1>, 2016.





- Gray, S. L. and Dacre, H. F.: Classifying dynamical forcing mechanisms using a climatology of extratropical cyclones, *Quart. J. Roy. Meteorol. Soc.*, 132, 1119–1137, <https://doi.org/https://doi.org/10.1256/qj.05.69>, 2006.
- 655 Griffiths, M., Thorpe, A. J., and Browning, K. A.: Convective destabilization by a tropopause fold diagnosed using potential-vorticity inversion, *Quart. J. Roy. Meteorol. Soc.*, 126, 125–144, <https://doi.org/https://doi.org/10.1002/qj.49712656207>, 2000.
- Gómez, B., Charlton-Pérez, C. L., Lewis, H., and Candy, B.: The Met Office Operational Soil Moisture Analysis System, *Remote Sens.*, 12, <https://doi.org/10.3390/rs12223691>, 2020.
- 660 Hardy, S., Methven, J., Schwendike, J., Harvey, B., and Cullen, M.: Examining the dynamics of a Borneo vortex using a balance approximation tool, *EGUsphere*, 2023, 1–31, <https://doi.org/10.5194/egusphere-2023-1312>, 2023.
- Hart, R. E.: A Cyclone Phase Space Derived from Thermal Wind and Thermal Asymmetry, *Mon. Weather Rev.*, 131, 585 – 616, [https://doi.org/10.1175/1520-0493\(2003\)131<0585:ACPSDF>2.0.CO;2](https://doi.org/10.1175/1520-0493(2003)131<0585:ACPSDF>2.0.CO;2), 2003.
- Harvey, B., Methven, J., Sanchez, C., and Schafner, A.: Diabatic generation of negative potential vorticity and its impact on the North Atlantic jet stream, *Quart. J. Roy. Meteorol. Soc.*, 146, 1477–1497, <https://doi.org/10.1002/qj.3747>, 2020.
- 665 Heming, J. T.: Met Office Unified Model Tropical Cyclone Performance Following Major Changes to the Initialization Scheme and a Model Upgrade, *Weather Forecast.*, 31, 1433 – 1449, <https://doi.org/10.1175/WAF-D-16-0040.1>, 2016.
- Heming, J. T.: Tropical cyclone tracking and verification techniques for Met Office numerical weather prediction models, *Meteorol. Appl.*, 24, 1–8, <https://doi.org/10.1002/met.1599>, 2017.
- 670 Hersbach, H., Bell, B., Berrisford, P., Hirahara, S., Horányi, A., Muñoz-Sabater, J., Nicolas, J., Peubey, C., Radu, R., Schepers, D., Simmons, A., Soci, C., Abdalla, S., Abellan, X., Balsamo, G., Bechtold, P., Biavati, G., Bidlot, J., Bonavita, M., De Chiara, G., Dahlgren, P., Dee, D., Diamantakis, M., Dragani, R., Flemming, J., Forbes, R., Fuentes, M., Geer, A., Haimberger, L., Healy, S., Hogan, R. J., Hólm, E., Janisková, M., Keeley, S., Laloyaux, P., Lopez, P., Lupu, C., Radnoti, G., de Rosnay, P., Rozum, I., Vamborg, F., Villaume, S., and Thépaut, J.-N.: The ERA5 global reanalysis, *Quart. J. Roy. Meteorol. Soc.*, 146, 1999–2049, <https://doi.org/10.1002/qj.3803>, 2020.
- 675 Hitchman, M. H. and Rowe, S. M.: On the Similarity of Lower-Stratospheric Potential Vorticity Dipoles above Tropical and Midlatitude Deep Convection, *J. Atmos. Sci.*, 74, 2593 – 2613, <https://doi.org/10.1175/JAS-D-16-0239.1>, 2017.
- Homar, V., Romero, R., Stensrud, D. J., Ramis, C., and Alonso, S.: Numerical diagnosis of a small, quasi-tropical cyclone over the western Mediterranean: Dynamical vs. boundary factors, *Quart. J. Roy. Meteorol. Soc.*, 129, 1469–1490, <https://doi.org/10.1256/qj.01.91>, 2003.
- Hoskins, B. J. and Hodges, K. I.: New Perspectives on the Northern Hemisphere Winter Storm Tracks, *J. Atmos. Sci.*, 59, 1041 – 1061, [https://doi.org/10.1175/1520-0469\(2002\)059<1041:NPOTNH>2.0.CO;2](https://doi.org/10.1175/1520-0469(2002)059<1041:NPOTNH>2.0.CO;2), 2002.
- 680 Hou, A. Y., Kakar, R. K., Neeck, S., Azarbarzin, A. A., Kummerow, C. D., Kojima, M., Oki, R., Nakamura, K., and Iguchi, T.: The Global Precipitation Measurement Mission, *Bull. Amer. Meteorol. Soc.*, 95, 701 – 722, <https://doi.org/10.1175/BAMS-D-13-00164.1>, 2014.
- Keller, J. H., Grams, C. M., Riemer, M., Archambault, H. M., Bosart, L., Doyle, J. D., Evans, J. L., Galarneau, T. J., Griffin, K., Harr, P. A., Kitabatake, N., McTaggart-Cowan, R., Pantillon, F., Quinting, J. F., Reynolds, C. A., Ritchie, E. A., Torn, R. D., and Zhang, F.: The Extratropical Transition of Tropical Cyclones. Part II: Interaction with the Midlatitude Flow, Downstream Impacts, and Implications for Predictability, *Mon. Weather Rev.*, 147, 1077 – 1106, <https://doi.org/10.1175/MWR-D-17-0329.1>, 2019.
- 685 Khodayar, S., Kalthoff, N., and Kottmeier, C.: Atmospheric conditions associated with heavy precipitation events in comparison to seasonal means in the western mediterranean region, *Clim. Dynam.*, 51, 1432–0894, <https://doi.org/10.1007/s00382-016-3058-y>, 2018.
- Lagouvardos, K., Karagiannidis, A., Dafis, S., Kalimeris, A., and Kotroni, V.: Ianos—A Hurricane in the Mediterranean, *Bull. Amer. Meteorol. Soc.*, 103, E1621 – E1636, <https://doi.org/10.1175/BAMS-D-20-0274.1>, 2022.
- 690



- Lfarh, W., Pantillon, F., and Chaboureau, J.-P.: The downward transport of strong wind by convective rolls in a Mediterranean windstorm, *Monthly Weather Review*, <https://doi.org/https://doi.org/10.1175/MWR-D-23-0099.1>, 2023.
- Lionello, P., Conte, D., and Reale, M.: The effect of cyclones crossing the Mediterranean region on sea level anomalies on the Mediterranean Sea coast, *Nat. Hazards Earth Syst. Sci.*, 19, 1541–1564, <https://doi.org/10.5194/nhess-19-1541-2019>, 2019.
- 695 Mahmood, S., Lewis, H., Arnold, A., Castillo, J., Sanchez, C., and Harris, C.: The impact of time-varying sea surface temperature on UK regional atmosphere forecasts, *Met. Appl.*, 28, e1983, <https://doi.org/10.1002/met.1983>, 2021.
- Manners, J., Edwards, J. M., Hill, P., and Thelen, J.-C.: SOCRATES (Suite Of Community RAdiative Transfer codes based on Edwards and Slingo) Technical Guide, <https://code.metoffice.gov.uk/trac/socrates>, last accessed 19-October-2023, 2018.
- Mazza, E., Ulbrich, U., and Klein, R.: The Tropical Transition of the October 1996 Medicane in the Western Mediterranean Sea: A Warm  
700 Seclusion Event, *Mon. Weather Rev.*, 145, 2575 – 2595, <https://doi.org/10.1175/MWR-D-16-0474.1>, 2017.
- Miglietta, M. M., Moscatello, A., Conte, D., Mannarini, G., Lacorata, G., and Rotunno, R.: Numerical analysis of a Mediterranean ‘hurricane’ over south-eastern Italy: Sensitivity experiments to sea surface temperature, *Atmos. Res.*, 101, 412–426, <https://doi.org/10.1016/j.atmosres.2011.04.006>, 2011.
- Miglietta, M. M., Laviola, S., Malvaldi, A., Conte, D., Levizzani, V., and Price, C.: Analysis of tropical-like cyclones over the Mediterranean  
705 Sea through a combined modeling and satellite approach, *Geophys. Res. Lett.*, 40, 2400–2405, <https://doi.org/10.1002/grl.50432>, 2013.
- Miglietta, M. M., Cerrai, D., Laviola, S., Cattani, E., and Levizzani, V.: Potential vorticity patterns in Mediterranean “hurricanes”, *Geophys. Res. Lett.*, 44, 2537–2545, <https://doi.org/10.1002/2017GL072670>, 2017.
- Navarro, A., García-Ortega, E., Merino, A., Sánchez, J. L., Kummerow, C., and Tapiador, F. J.: Assessment of IMERG Precipitation Estimates over Europe, *Remote Sens.*, 11, <https://doi.org/10.3390/rs11212470>, 2019.
- 710 NCAS British Atmospheric Data Centre: Meteosat Second Generation (MSG) Geostationary Satellites: Visible, Infra-Red and Water Vapour Images and Derived Data Products over the world, <http://catalogue.ceda.ac.uk/uuid/5fa2529b973e47ae38ab3557f2018ef4>, accessed on April 3, 2023, 2006.
- Noyelle, R., Ulbrich, U., Becker, N., and Meredith, E. P.: Assessing the impact of sea surface temperatures on a simulated medicane using ensemble simulations, *Nat. Hazards Earth Syst. Sci.*, 19, 941–955, <https://doi.org/10.5194/nhess-19-941-2019>, 2019.
- 715 Oertel, A., Boettcher, M., Joos, H., Sprenger, M., and Wernli, H.: Potential vorticity structure of embedded convection in a warm conveyor belt and its relevance for large-scale dynamics, *Weather Clim. Dynam.*, 1, 127–153, <https://doi.org/10.5194/wcd-1-127-2020>, 2020.
- Plant, R. S., Craig, G. C., and Gray, S. L.: On a threefold classification of extratropical cyclogenesis, *Quart. J. Roy. Meteorol. Soc.*, 129, 2989–3012, <https://doi.org/https://doi.org/10.1256/qj.02.174>, 2003.
- Raveh-Rubin, S. and Wernli, H.: Large-scale wind and precipitation extremes in the Mediterranean: a climatological analysis for 1979–2012,  
720 *Quarterly Journal of the Royal Meteorological Society*, 141, 2404–2417, <https://doi.org/https://doi.org/10.1002/qj.2531>, 2015.
- Ricchi, A., Miglietta, M. M., Barbariol, F., Benetazzo, A., Bergamasco, A., Bonaldo, D., Cassardo, C., Falcieri, F. M., Modugno, G., Russo, A., Sclavo, M., and Carniel, S.: Sensitivity of a Mediterranean Tropical-Like Cyclone to Different Model Configurations and Coupling Strategies, *Atmosphere*, 8, <https://doi.org/10.3390/atmos8050092>, 2017.
- Roberts, N.: A guide to aspects of water vapour imagery interpretation: the significance of dry region, Met Office, Meteorology Research  
725 and Development, Tech. Report No. 109, 2000.
- Rotunno, R. and Emanuel, K. A.: An Air–Sea Interaction Theory for Tropical Cyclones. Part II: Evolutionary Study Using a Nonhydrostatic Axisymmetric Numerical Model, *J. Atmos. Sci.*, 44, 542 – 561, [https://doi.org/10.1175/1520-0469\(1987\)044<0542:AAITFT>2.0.CO;2](https://doi.org/10.1175/1520-0469(1987)044<0542:AAITFT>2.0.CO;2), 1987.



- Sakib, S., Ghebreyesus, D., and Sharif, H. O.: Performance Evaluation of IMERG GPM Products during Tropical Storm Imelda, *Atmosphere*, 12, <https://doi.org/10.3390/atmos12060687>, 2021.
- 730
- Sardeshmukh, P. D. and Hoskins, B. I.: Spatial Smoothing on the Sphere, *Mon. Weather Rev.*, 112, 2524 – 2529, [https://doi.org/https://doi.org/10.1175/1520-0493\(1984\)112<2524:SSOTS>2.0.CO;2](https://doi.org/https://doi.org/10.1175/1520-0493(1984)112<2524:SSOTS>2.0.CO;2), 1984.
- Saunders, R., Hocking, J., Turner, E., Rayer, P., Rundle, D., Brunel, P., Vidot, J., Roquet, P., Matricardi, M., Geer, A., Bormann, N., and Lupu, C.: An update on the RTTOV fast radiative transfer model (currently at version 12), *Geosci. Model Dev.*, 11, 2717–2737, <https://doi.org/10.5194/gmd-11-2717-2018>, 2018.
- 735
- Short, C. J. and Petch, J.: How Well Can the Met Office Unified Model Forecast Tropical Cyclones in the Western North Pacific?, *Weather Forecast.*, 33, 185 – 201, <https://doi.org/10.1175/WAF-D-17-0069.1>, 2018.
- Skofronick-Jackson, G., Petersen, W. A., Berg, W., Kidd, C., Stocker, E. F., Kirschbaum, D. B., Kakar, R., Braun, S. A., Huffman, G. J., Iguchi, T., Kirstetter, P. E., Kummerow, C., Meneghini, R., Oki, R., Olson, W. S., Takayabu, Y. N., Furukawa, K., and Wilheit, T.: The Global Precipitation Measurement (GPM) Mission for Science and Society, *Bull. Amer. Meteorol. Soc.*, 98, 1679 – 1695, <https://doi.org/https://doi.org/10.1175/BAMS-D-15-00306.1>, 2017.
- 740
- Smith, R. N. B.: A scheme for predicting layer clouds and their water content in a general circulation model, *Quart. J. Roy. Meteorol. Soc.*, 116, 435–460, <https://doi.org/10.1002/qj.49711649210>, 1990.
- Stathopoulos, C., Patlakas, P., Tsalis, C., and Kallos, G.: The Role of Sea Surface Temperature Forcing in the Life-Cycle of Mediterranean Cyclones, *Remote Sens.*, 12, <https://doi.org/10.3390/rs12050825>, 2020.
- 745
- Sánchez, C., Methven, J., Gray, S., and Cullen, M.: Linking rapid forecast error growth to diabatic processes, *Quart. J. Roy. Meteorol. Soc.*, 146, 3548–3569, <https://doi.org/10.1002/qj.3861>, 2020.
- Tennant, W. and Beare, S.: New schemes to perturb sea-surface temperature and soil moisture content in MOGREPS, *Quart. J. Roy. Meteorol. Soc.*, 140, 1150–1160, <https://doi.org/10.1002/qj.2202>, 2014.
- 750
- Wernli, H. and Schwierz, C.: Surface Cyclones in the ERA-40 Dataset (1958–2001). Part I: Novel Identification Method and Global Climatology, *J. Atmos. Sci.*, 63, 2486 – 2507, <https://doi.org/10.1175/JAS3766.1>, 2006.
- Wilson, D. R. and Ballard, S. P.: A microphysically based precipitation scheme for the UK meteorological office unified model, *Quart. J. Roy. Meteorol. Soc.*, 125, 1607–1636, <https://doi.org/10.1002/qj.49712555707>, 1999.
- Wood, N., Staniforth, A., White, A., Allen, T., Diamantakis, M., Gross, M., Melvin, T., Smith, C., Vosper, S., Zerroukat, M., and Thuburn, J.: An inherently mass-conserving semi-implicit semi-Lagrangian discretization of the deep-atmosphere global non-hydrostatic equations, *Quart. J. Roy. Meteorol. Soc.*, 140, 1505–1520, <https://doi.org/10.1002/qj.2235>, 2014.
- 755
- Zerroukat, M. and Shipway, B. J.: ZLF (Zero Lateral Flux): a simple mass conservation method for semi-Lagrangian-based limited-area models, *Quart. J. Roy. Meteorol. Soc.*, 143, 2578–2584, <https://doi.org/10.1002/qj.3108>, 2017.
- Zimbo, F., Ingemi, D., and Guidi, G.: The Tropical-like Cyclone “Ianos” in September 2020, *Meteorology*, 1, 29–44, <https://doi.org/10.3390/meteorology1010004>, 2022.
- 760
- Čampa, J. and Wernli, H.: A PV Perspective on the Vertical Structure of Mature Midlatitude Cyclones in the Northern Hemisphere, *J. Atmos. Sci.*, 69, 725 – 740, <https://doi.org/https://doi.org/10.1175/JAS-D-11-050.1>, 2012.